Wear 593 (2026) 206611

Contents lists available at ScienceDirect

Wear

journal homepage: www.elsevier.com/locate/wear

Erosion-corrosion performance of nickel-aluminium bronze alloys in marine environments: recent developments

Robert JK. Wood *, Julian A. Wharton

National Centre for Advanced Tribology at Southampton (nCATS), Department of Mechanical Engineering, School of Engineering, Faculty of Engineering and Physical Sciences, University of Southampton, SO17 1BJ, UK

ARTICLE INFO

Keywords:
Nickel-aluminium bronze
Cavitation
Erosion-corrosion
Synergy
Marine
Surface oxides

ABSTRACT

Nickel-aluminium bronze (NAB) plays a critical role in seawater cooling of power stations, marine propulsion, and offshore energy applications. As the marine industry advances toward net-zero emissions and decarbonisation, extending asset lifetimes and improving energy efficiency have become essential. Despite casting standards designed to minimise selective phase attack, NAB often underperforms under erosion-corrosion conditions, particularly in environments involving cavitation and solid particle loading, leading to premature component failure, costly maintenance, and reduced operational efficiency. This review critically examines recent research on erosion-corrosion performance of NAB alloys, with a focus on surface condition and surface-environment interactions that govern degradation mechanisms. It highlights the influence of pre-conditioning treatments (*e.g.*, shot peening, long-term seawater immersion), the resultant compressive residual surface stresses, and the role of oxide film formation in mitigating surface damage. The review also evaluates the impact of deposition techniques, including surface welding, friction stir welding, and explores the effects of alloying additions, such as chromium (Cr) and rare earth elements (Ce, Sm and Yb) on corrosion resistance and mechanical integrity. Additionally, it assesses the performance of coated NAB and associated nickel-based alloys being considered as alternative for geothermal applications. By assessing both cavitation and slurry erosion-corrosion studies, this review identifies key microstructural factors, such as κ-phase distribution, galvanic coupling, and work hardening, that influence synergy between mechanical and corrosion degradation. It also provides fresh insight into the urgent need for standardisation test protocol to enable meaningful comparisons across alloy variants and environmental conditions. Ultimately, this review provides guidance for the design and optimisation of NAB components for high performance, low-maintenance operation in aggressive marine environments.

1. Introduction

Aluminium bronzes are copper-based alloys known for their excellent mechanical properties and corrosion resistance [1]. Both cast and wrought forms have served reliably in a variety of marine applications for decades, finding application in components such as valves and fittings, ship propellers, pump castings, pump shafts, valve stems and heat exchanger waterboxes [2]. Among these, nickel–aluminium bronze (NAB) alloys, which typically contain 9–12 wt% aluminium with up to 6 wt% each of iron and nickel, represent one of the commercially significant systems. NAB alloys exhibit complex metallurgy with several intermetallic phases, in which small variations in composition can result in the development of markedly different microstructures [3–5], which in turn result in wide variations in seawater corrosion resistance. The microstructures that result in optimum corrosion resistance can be obtained by controlling the composition and heat treatment [6]. For example, naval grade CuAl9Ni5Fe4Mn castings undergo an annealing treatment NES747 Part 2 at 675 °C for a minimum period of 6 h to refine their microstructure (limiting the β-phase) [7,8].

The microstructure of a sand cast NAB (Fig. 1a) reveals light etched areas of α-phase, which is a fcc copper-rich solid solution and dark etched martensitic regions (β′-phase) or retained β - a high temperature phase, surrounded by lamellar eutectoid phases and several intermetallic κ-phases. The κ_I-phase is either globular or rosette shaped and iron-rich (based on Fe_3Al). The κ_{II}-phase forms dendritic rosettes which are unevenly distributed at the α/β boundary interface and are smaller than

This article is part of a special issue entitled: Tribocorrosion_invited only published in Wear.

* Corresponding author.
E-mail address: r.wood@soton.ac.uk (R.JK. Wood).

https://doi.org/10.1016/j.wear.2026.206611
Received 10 October 2025; Received in revised form 9 January 2026; Accepted 19 February 2026
Available online 27 February 2026

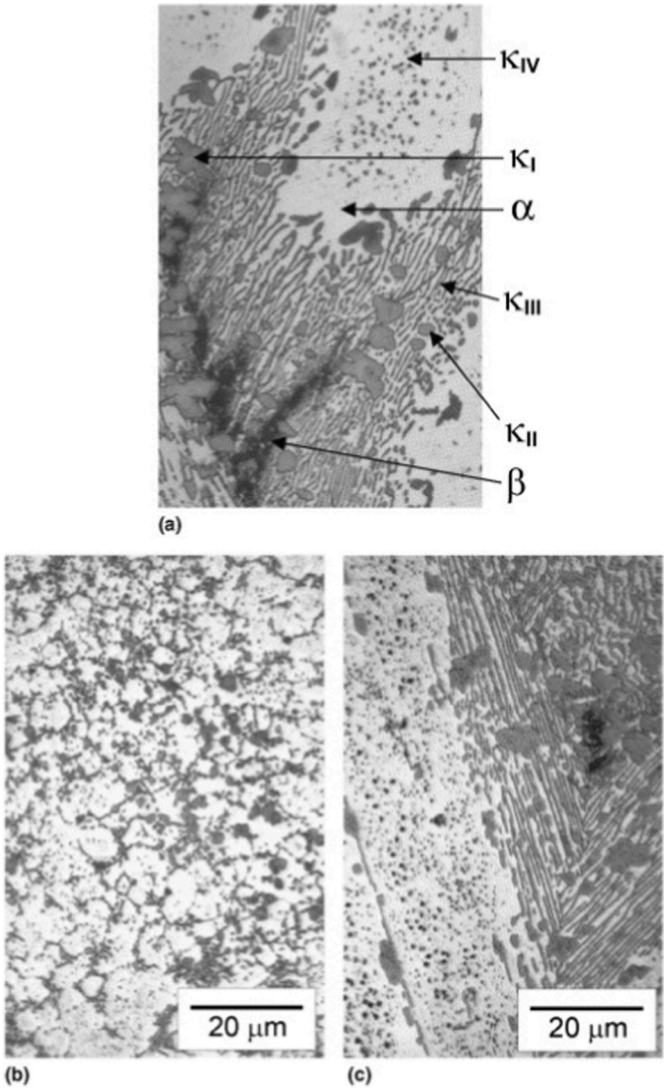

Fig. 1. Optical micrographs of nickel-aluminium bronze: **(a)** sand cast NAB, **(b)** wrought bar NAB, and **(c)** British Naval specification, cast then annealed (NES 747 Part 2) reproduced from Ref. [1].

the κ_I rosette. The κ_{III}-phase can appear in either a lamellar or sometimes a coagulated or globular (degraded lamellar) form. It grows normal to the α/β boundary, as well as forming at the boundary of the large κ_I-phase and is nickel-rich (NiAl). The κ_{IV}-phase is a fine precipitate within the α-phase and is iron-rich. In contrast, the microstructure of a wrought NAB (Fig. 1b), viewed perpendicular to the extrusion direction, shows significant influence due to the extrusion process, suppressing the formation of the β and κ_{III}-phases. The NES747 Part 2 British Naval standard prescribes a heat treatment that minimises or eliminates of the more corrosion prone β-phase, while promoting a dense distribution of fine κ-phase precipitates in the α-phase [8], see Fig. 1c, thereby enhancing the corrosion resistance.

NAB corrosion resistance has been attributed to the formation of a protective layer, which requires time to develop and become effective. The layer typically ranges from 900 to 1000 nm in thickness and is composed primarily of aluminium and copper oxides [9,10]. It exhibits a compositional gradient: the oxide layer is aluminium-rich adjacent to the metal interface, while richer in copper towards the outer surfaces. Over time, especially with prolonged seawater exposure, the film also incorporates nickel and iron oxides, along with trace amounts of copper salts and hydroxychlorides such as $Cu_2(OH)_3Cl$ and Cu(OH)Cl. The oxide layer, interlocked with intermetallic κ-phases, adheres firmly to the base metal surface and significantly reduces corrosion rates by a factor of 20–30 [9]. The protective effect arises from two key mechanisms: suppression of anodic metal dissolution by impeding ionic transport across the oxide layer, and reduction of cathodic reaction kinetics on the oxide surface [10]. In marine environments, whether quiet, tidal or moderately flowing seawater (provided flow velocity does not exceed 2.7 m s^{-1} [11]), the protective film continues to mature leading to improve corrosion performance. Eventually, the long-term corrosion rate stabilises between 0.015 and 0.05 mm y^{-1} (0.6–2.0 μA cm^{-2}) [3,12]. Among copper-based alloys, NAB is considered the most resistant to flow-induced corrosion. However, under high-velocity or turbulent service conditions, the protective oxide layer can suffer mechanical damage, locally exposing the underlying bare metal. NAB becomes increasingly vulnerable in seawater when flow velocities exceed 4.3 m s^{-1} and the degree of attack is reported to vary logarithmically with velocity: from 0.5 mm y^{-1} (20 μA cm^{-2}) at 7.6 m s^{-1} to 0.76 mm y^{-1} (31 μA cm^{-2}) at 30.5 m s^{-1}. In some cases, corrosion rates can locally reach up to 2 mm y^{-1}, even at 7.6 m s^{-1} [13].

Meigh [3] identifies sulphides as a primary threat to copper based alloys, particularly aluminium bronze, in certain fresh and seawater environments. Sulphides act as strong reducing agents, reacting with protective surface oxides to form a porous, loosely adherent copper sulphide films that offer limited resistance to both corrosion and erosion. Studies on pure copper [14,15], copper-nickel alloy [16–18] and aluminium bronzes [19] consistently report this degradation effect. These films lack mechanical integrity and can be stripped away under flowing conditions. Due to its porous structure, the sulphide film allows dissolved oxygen to penetrate, which accelerates corrosion by facilitating both anodic and cathodic reactions. Components handling sulphide and oxygen containing water, such as pumps and valves, are especially susceptible to this form of degradation. As previously discussed, the erosion-corrosion performance of NAB alloys strongly depends on their microstructure-composition. Consequently, the manufacturing route, post-processing treatments (such as heat or laser treatments) and the type of surface coating, if deposited, all play crucial roles in determining the alloy's erosion-corrosion performance.

There are several types of erosion-corrosion with Fig. 2 visualising the various possible erosion-corrosion interactions. The review will focus on these.

With the decarbonisation agenda accelerating life-extension programmes for critical marine infrastructure (maritime propulsion and seawater handling, power generation, etc.) and increasing duty cycles in cavitating, particle-laden flows, erosion-corrosion of NAB has become a primary constraint on reliability and energy efficiency across marine and power sectors. Concurrently, rapid advances in surface conditioning, deposition routes, and Cr/rare-earth alloying, alongside growing

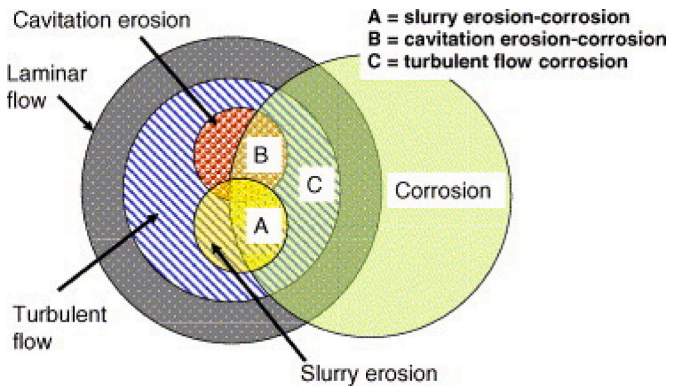

Fig. 2. Venn diagram illustrating the possible regions of erosion–corrosion interactions between different flow regimes and corrosion: (A) slurry erosion–corrosion, (B) cavitation erosion–corrosion and (C) turbulent flow or flow enhanced erosion–corrosion [20].

interest in geothermal brines, have outpaced test standardisation, making a synthesis of mechanisms and harmonised protocols urgently needed to guide robust design and maintenance.

This review explores how manufacturing processes influence the performance of NAB, with particular attention to selective phase attack and the impact of service environments, including the effects of sulphide concentration in the electrolyte. The role of anodic phase corrosion and microstructure degradation in tribocorrosion are also discussed, alongside an outline of the current state-of-the-art and understanding of erosion-corrosion of cast NAB. The review will assess slurry, cavitation, pipe flow and jet impingement erosion-corrosion of NAB. The performance of the various NAB types and coatings are discussed for each test type, with emphasis on their microstructural characteristics and interrelationships. Data from recent literature are used to rank the performance of NAB surfaces produced via various manufacturing and deposition methods. These rankings are correlated with updated synergy values, mapped against the ratio of mechanical to electrochemical contributions to surface material loss. The review concludes on future research directions. In so doing, the review addresses environmental conditions, alloy microstructure and composition, surface modification and deposition techniques, and mapping of synergistic effect in studies that quantify interaction between mechanical and electrochemical degradation. It also presents recent findings by the authors and others on cavitation erosion-corrosion under alternating static and dynamic seawater conditions, mimicking the operational cycles of marine propulsion systems, and examines the implications for long term immersion periods. Ultimately, the review emphasizes the importance of understanding the interplay between mechano-electrochemical-microstructural mechanisms. The NAB surfaces examined include those produced by as-cast, forged, welded, friction stir processed, shot peening, heat treated, powder metallurgy, rare earth additions, chromium additions, and hot extrusion. Additionally, laser surface modified manganese aluminium bronze (MAB) has been investigated, as along with coating techniques for NAB such as electrodeposition, cold metal transfer, and direct energy deposition.

This review therefore aims to:

- Examine how manufacturing processes influence the performance of NAB and how service environments affect degradation;
- Surmarise research on slurry, cavitation, pipe flow and jet impingement erosion-corrosion of NAB;
- Explore approaches for mapping interactions between mechanical and electrochemical contributions (synergy and antagonism);
- Assess the impact of alternating static and dynamic seawater conditions, representative of marine propulsion system operation.

The review considers 25 papers published over the past 15 years on the tribocorrosion of NAB and related marine alloys. Of these, twelve papers quantify synergy, nine focus on cavitation erosion-corrosion and seven on slurry erosion-corrosion, one on jet impingement and two on pipe flow. Most studies concentrate on fundamental tribocorrosion mechanisms rather than on service relevant materials and conditions.

The review is structured as follows. It first outlines the need for a review tribocorrosion-focussed assessment of NABs, defines synergy, and summarises the manufacturing processes and compositions of bronzes examined. It then covers corrosion behaviour induce under seawater immersion, followed by the various erosion-corrosion modes (cavitation, slurry, jet impingement and pipe flow). Each section describes material performance and a dedicated section addressing microstructure-performance interactions. A further section reviews the performance of related marine materials and coatings under cavitation erosion-corrosion. The review then maps synergistic levels for the studies that quantify synergy and discusses the synergistic mechanisms responsible for enhanced material loss. It concludes with a summary of key findings.

Experimental data within the reviewed studies was obtained from mass loss measurements and corrosion currents determined by electrochemical polarisation, with Faradaic conversion used to estimate mass loss. Electrochemical impedance spectroscopy (EIS) was employed in studies that investigated surface films in greater detail.

1.1. Synergy

When erosion (E) and corrosion (C) occur simultaneously, their interaction typically accelerates material degradation through a mechano-electrochemical mechanism. In such cases, the total material loss (T) from the surface is not simply the sum of erosion and corrosion losses. Instead, it includes an addition term, synergy (S), which typically accounts for the enhanced degradation due to their interaction (*i.e.*, $T = E + C + S$). In some cases, negative synergy or antagonism is reported. Quantifying this synergy is essential for predicting component failure and optimising service life service in aggressive erosive environments. Synergy is evaluated by measuring the total mass loss under combined erosion and corrosion conditions [21], capturing the non-linear interaction between mechanical wear and electrochemical corrosion, and can provide insights into the coupled degradation mechanisms, expressed as Equation (1) [1].

$$S = T - (E + C) = \Delta E_C + \Delta C_E \tag{1}$$

where S represents the total material loss resulting from synergistic interactions between mechanical wear and electrochemical corrosion. T is the total measured material loss under erosion-corrosion conditions. E indicates the material degradation due solely to mechanical erosive wear, measured in the absence of any corrosion mechanisms. C denotes the material damage caused exclusively by corrosion, measured under a non-erosive condition. ΔE_C is the enhanced erosion caused by corrosion and ΔC_E is the enhanced corrosion caused by erosion. Another way to express the significance of the synergy term is through the magnifying factor (M), which quantifies how much the total loss under combined erosion-corrosion conditions exceeds the sum of the individual losses due to erosion and corrosion alone. M is defined as:

$$M = \frac{T}{(E + C)} \tag{2}$$

Where M is the magnifying factor, a dimensionless quantity. A value of $M > 1$ indicates a synergistic interaction, where the combined effect of erosion and corrosion is greater than their individual contributions. This metric provides a practical means to assess the severity of mechano-electrochemical interactions and to compare the performance of differential alloys or surface treatments under aggressive in-service conditions.

1.2. Materials reviewed

Table 1 lists the composition of the materials reported in the various references cited in this review and Fig. 3 graphically illustrates these compositions to aid comparison. Although the NAB alloys tested broadly follow the expected compositions to facilitate comparison, noticeable deviations do occur. Unfortunately, the inconsistent reporting of mechanical properties in the source papers makes it difficult to assess the significance of these compositional variations. Table 7 shows micrographs of both untested and tested microstructures of these materials. However, inconsistencies in magnification and in the imaging techniques used (optical *vs.* electron microscopy) for the initial and damaged microstructures make meaningful comparisons across studies impossible.

Table 1
Composition of materials studied wt. (%).

Data no.	Ref.	Test	Al	Ni	Fe	Mn	Zn	Si	Cr	Re	Cu	Notes
0	[22]	Slurry jet										Cast NAB, No composition given
1	[2,19]	Cav ASTM G32	9.3	4.5	4.88	0.97					Bal.	Cast NAB and CAST MAB
2	[7]	Cav ASTM G32	9.25	4.4	4.6	1.35				0.03	Bal.	Cast NAB
3	[4]	Cav ASTM G32	11.58	3.98	5.12	0.09					Bal.	Cast NAB
4	[5]	Cav ASTM G32	11.58	3.98	5.12	0.09	0.43				Bal.	Cast NAB
5	[6]	Immersion	9.14	4.84	4.38	0.09					Bal.	Cast NAB to NES 747
6	[23]	Slurry pot	9.9	5.6	3.5	1.2					Bal.	Friction Stir Processed and cast NAB
7	[24]	Pipe-flow	9	4.5	4	1					Bal.	Cast NAB
8	[24]	Pipe-flow	9	4.5	4	1			0.3		Bal.	Cast NAB-Cr
9	[25]	Cav ASTM G32	9.66	4.66	4.45	2.19					Bal.	Cast NAB
10	[26]	Cav ASTM G73–10	9.42	3.73	4.3	0.94					Bal.	Cast NAB
11	[27]	Tubular flow	9	4.6	4.1	1.2					Bal.	Cast NAB
12	[21, 28]	Cav ASTM G32	9.14	4.84	4.38	0.09					Bal.	Cast NAB to NES 747
13	[29]	Slurry pot	1.66	0.014	0.087	2.87	34.85	0.78				RB031 Manganese-Silicon Brass
14	[29]	Slurry pot	4.83	2.42	3.43	2.73	22.1	2.42				RB032 Manganese-Silicon Brass
15	[30]	Cav ASTM G32	8.9	4.38	3.31	1.49					Bal.	Cast NAB and Directed energy deposited DED NAB
16	[31]	Slurry erosion	10.06	3.633	4.02	0.25					Bal.	Cast NAB and shot peened (SP) NAB
17	[32]	Cav ASTM G32	4.66	1.64	1.98	8.63					Bal.	Cast MAB
18	[33]	Cav ASTM G32	8.84	4.56	4.52	2.41					Bal.	Cast NAB
19	[34]	Cav ASTM G32	10.75	4.5	6	2.3					Bal.	Forged NAB
20	[34]	Cav ASTM G32	10.5	4.3	5.6	1.6					Bal.	Cast NAB
21	[35]	Jet impingement	9.85	3.76	3.86	1.03					Bal.	Cast NAB
22	[36]	pipe-flow	9.11	4.46	4.1	10.4					Bal.	Cast NAB and hot extruded NAB
23	[37]	Vibratory cav but not to ASTM	10.3	4.05	4.26	1.34					Bal.	Cast NAB and Friction Stir Processed (FSP) NAB
24	[38]	Slurry pot	9.7	4.4	4.3	0.9					Bal.	Cast NAB
25	[38]	Slurry pot	10	5	4	1					Bal.	Powder Metallurgy (PM) NAB
26	[22]	Cav ASTM G32-10		Bal.	5	0.1		0.3	22		0.5	Coatings ERNiCrMo-3 (Inconel 625)
27	[37]	Cav ASTM G32-10		Bal.	6	0.8		0.08	16		0.5	ERNiCrMo-4 (Hastelloy C-276)
28	[39]	Jet impingement		11	1.9	0.7					Bal.	Cu-10Ni
29	[39]	Jet impingement	1.8	19	1	4			0.5		Bal.	High Strength Cu-Ni

Latest revised version: ASTM G32-16(2016)e1 [40].

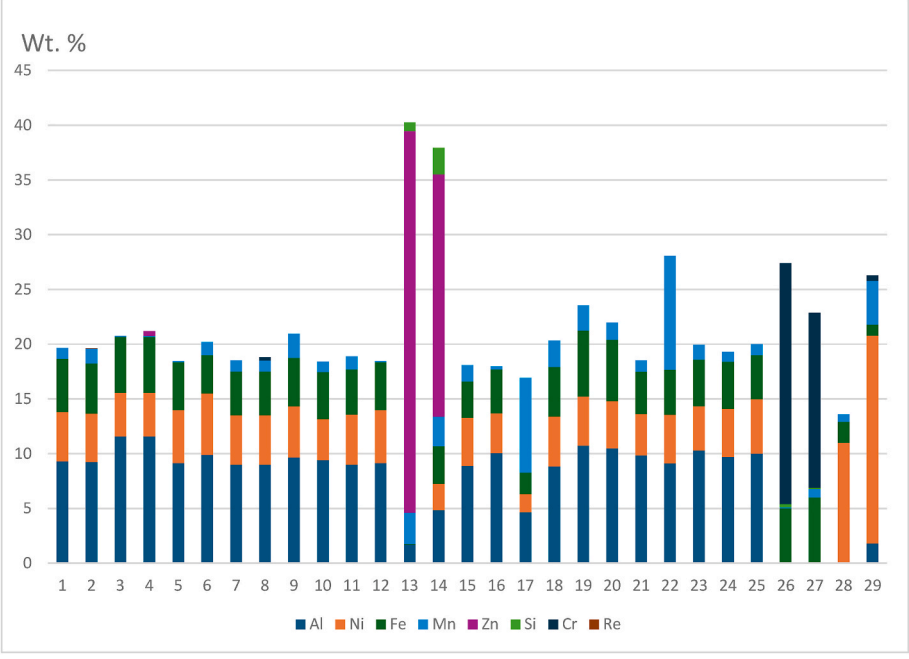

Fig. 3. Composition of main elements of materials studied taken in order from Table 1. The balance in wt.% is Cu except for point 26 and 27 which are coatings with the balance of Ni.

2. Corrosion and erosion-corrosion performance of NAB

2.1. Immersion in seawater

Immersion of NAB in natural marine environments can produce aggressive surface attack and this early-stage corrosion acceleration is important when assessing the long-term durability of NAB components. For example, NAB corrosion rates when immersed in seawater are known to vary over time. Dobson et al. [6] investigated the long-term corrosion behaviour of welded NAB through immersion tests conducted in natural seawater at Millbay Marina (Plymouth, UK), as well as in simulated seawater and air. Their findings revealed that NAB experienced an initial accelerated corrosion rate of 1.27 mm y^{-1} during the first few months of exposure in natural seawater. Over time, this rate decreased and stabilised to 0.11 mm y^{-1} (annual average). This long-term rate was nearly double the 0.06 mm y^{-1} observed in simulated seawater and approximately 30 times higher than corrosion rate measured to air.

2.2. Slurry erosion-corrosion

This section reviews recent research on slurry erosion-corrosion performance for NAB and that look at reducing overall damage rates by using different surface treatments such as peening, laser treatment and quenching. To aid interpretation of the results, the kinetic energy E_k of the impacting particles, which governs the severity of the mechanical damage, is given by:

$$E_k = \frac{1}{2}\left(\frac{4}{3}\pi\rho r^3\right)(\nu^2) \tag{3}$$

Where ρ is the density of the particle, r is the radius of the particle (assumed spherical), ν is the velocity of the particle.

Slurry jet impingement erosion-corrosion performance of laser processed NAB with that of as-cast NAB is reported by Lakshminarayanan et al. [41]. As expected, results show that erosion-corrosion rates increased with jet velocity (i.e., the kinetic energy of the erodent, Equation (3)) but decreased as the slurry impact angle increased, indicating that ductile erosion mechanisms dominated. Dutta et al. [23] investigated chromium reinforced NAB fabricated using friction stir process (FSP). Slurry erosion–corrosion tests revealed that FSP treated surfaces exhibited lower erosion and corrosion rates than the as-cast NAB, primarily due to improved mechanical properties. For both FSP-treated and as-cast NAB, erosion–corrosion rates increased as the impact angle decreased from 90° to 30°, again confirming the dominance of ductile erosion mechanisms. He et al. [26], investigated electroplated Ni-Al-Cu coatings applied to NAB alloy substrates. Their tests were conducted in a slurry pot using gravel particles (125-500 μm) at concentrations up to 30 g L^{-1}, with samples positioned between 30° and 90° to the flow of 3.5 wt% NaCl solution at ambient temperature. Linear flow velocities ranged from 4.7 to 28.2 m s^{-1}, corresponding to particle kinetic energies (E_k) between 0.006 and 2.44 μJ. The coatings formed a metallurgical bond with the base alloy and exhibited an equiaxed crystalline structure composed solely of the Ni_3Al phase. Degradation mechanisms for the Ni-Al-Cu coatings, consisted of fatigue-induced delamination and grain disintegration under alternating/cyclic stress.

Adjusting silicon content in high-tensile brass alloys has shown improved erosion-corrosion performance under varied slurry conditions [29]. This study systemically varied parameters such as slurry concentration, slurry velocity, and silica sand particle size. Microstructure analysis revealed that the RB031 and RB032 alloys (high strength manganese-silicon brass alloys from India) developed manganese silicide phases, whereas the NAB alloy exhibited iron-rich intermetallics. Among the tested materials, RB032 alloy consistently demonstrated superior resistance to erosion-corrosion across all test conditions. The effects shot peening the surface on the erosion-corrosion performance of NAB [31], shows that increasing the intensity of shot peening significantly alters the degradation mechanism. At lower intensities, material loss was dominated by ductile deformation coupled with selective phase corrosion. However, as peening intensity increased, the mechanism transitioned to brittle, cleavage-like fracture. This shift highlights the dominant role of strain-hardening capacity over other factors such as surface hardness, compressive residual stress, and surface roughness in governing erosion-corrosion performance. Understanding and optimising heat treatment effects on microstructure, mechanical properties, as well as corrosion and erosion–corrosion behaviour of a NAB is critical [35]. Tests conducted at velocities between 1 and 5 m s^{-1}, with an impact angle of 90°, 3.5 wt% NaCl solution, 200 μm sand size of at 3 wt % concentration, and 5 h exposure. The corresponding E_k values ranged between 0.006 and 0.14 μJ. The results are plotted against particle energy in Figure ww shows that the erosion rate increases with impact energy but not linearly. The authors note that the quenched specimen aged at a relative low temperature of 450 °C exhibits the highest hardness and contains the hardest β' phases with a low portion α-phase. Therefore, this specimen shows excellent resistance to plastic deformation induced by mechanical erosion. In contrast, the annealed specimen has the fewest hard β' phases and a softer α-phase, leading to greater erosion-induced deformation. As strengthening particles, the κ-phases play an important role in determining the mechanical properties of NAB alloys and thus their erosion and erosion-corrosion resistances. The κ-phases precipitated during heat treatment are able to maintain the alloy strength during the annealing process or increase strength during normalizing and ageing processes.

The manufacturing route and thus the microstructure of NAB that is generated is critically important to the overall tribocorrosion performance. New processing approaches, such as powder metallurgy offer promise [38]. Similarly, heat treatment steps such as annealing can significantly influence microstructure, corrosion behaviour and slurry erosion-corrosion resistance, see Fig. 4. In this study, silica sand particles were screened (i.e., sieved) to exclude those larger than 355 μm, and the base testing conditions included 3.5 wt% NaCl solution, 3 wt% sand concentration, a flow speed of 3.8 m s^{-1} and a 48 h test duration, with a calculated E_k of 0.43 μJ.

A summary of the slurry erosion-corrosion performance for NAB, based on studies that quantify it, is presented in Table 2. Most surface treatments applied to as cast NAB (peening, laser treatment, quenching) appear to reduce loss rates by roughly 30% compared to untreated as-

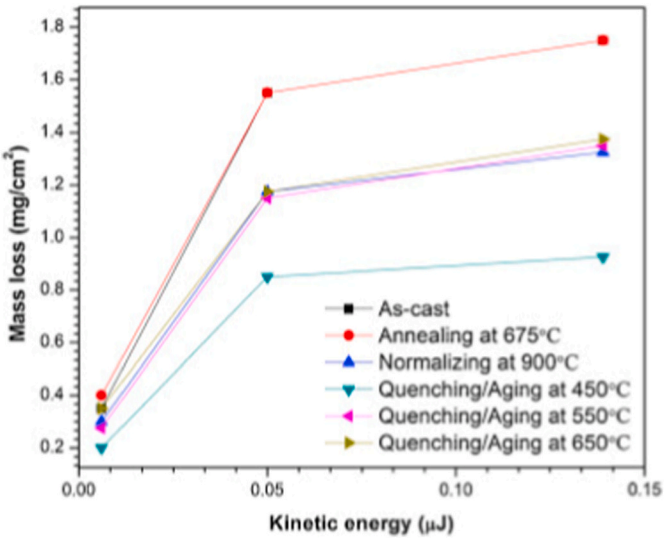

Fig. 4. Erosion rate, i.e., mass-loss, of NAB alloys under different heat treatments as a function of the impact kinetic energy in the deionized water with 3 wt% sand for 5 h [35].

Table 2
Slurry erosion-corrosion performance.

Reference/ data number	Test type	Materials	Erosion-corrosion performance
[31], DN16	Slurry erosion	Shot peened NAB	Optimal peening intensity, reduced mass loss rates by up to 30%
[23], DN6	Slurry pot	Chromium reinforced NAB fabricated using friction stir process (FSP)	FSP treated surfaces exhibited lower erosion and corrosion rates than the as-cast NAB
[41], DN0	Slurry jet impingement	Laser-processed NAB and as-cast NAB	Laser-processed NAB demonstrated a 28% improvement compared to as-cast NAB
[26], DN10	ASTM G73-10	Electroplated Ni-Al-Cu coatings applied to NAB	Reduction of 63-90% in material removal rate compared to uncoated NAB
[29], DN14	Slurry pot	High strength manganese-silicon alloys	RB032 showed 45% reduction in mass loss compared to as-cast NAB
[35], DN21	Impingement jet	Heat treated NAB	Quenching at 900 °C/ aging at 450 °C reduced mass loss by 33% compared to as-cast NAB
[38], DN24&25	Slurry pot	Powder metallurgy (PM) NAB	PM showed a 11% reduction in mass loss compared to as-cast NAB

cast NAB. Powder metallurgy processing yielded a more modest reduction of around 11%. In contrast, high strength manganese-silicon alloys and electroplated Ni-Al-Cu coatings applied to NAB demonstrated the most significant improvements, with reductions of 45 and up to 90%, respectively.

2.2.1. Microstructure-performance interactions during slurry erosion-corrosion

Microstructure-performance interactions are key to understand if damage rates are to be minimised. In Ref. [26], slurry erosion-corrosion testing of as-cast NAB revealed deformation and cracks, which led to the loss of hard κ- and β-phases, alongside deformation of the ductile α-phase. In a related study [35], examined the effects of heat treatment on as-cast NAB and found that the formation of hard phases such as β′ and κ-phases significantly improved the strength, hardness and erosion-corrosion resistance. While electrochemical corrosion behaviour remained largely unaffected by these microstructural changes, the improved erosion–corrosion resistance was attributed to the formation of these hard phases β′ and κ phases. Notably, all specimens exhibited negative synergy, suggesting that the presence of a protective oxide film reduced erosivity. Under erosion-only conditions, surfaces showed impact marks with plastic lips and micro-cracks, whereas under erosion-corrosion, these features were less pronounced, corroborating the reported dissolution of plastically deformed regions by corrosion [13,42,43]. The study also highlighted the importance of repassivation behaviour in mitigating surface damage during erosion-corrosion. Further work by Ref. [38] focused on NAB produced via powder metallurgy. The PM alloy had a course microstructure with more equiaxial α-phase grains and finer κ-precipitates, which collectively enhanced the erosion-corrosion resistance. The larger α-phase contributed to improved mechanical stability under slurry impact. In Ref. [29], the improved performance of high strength manganese-silicon alloys was attributed to their refined microstructure and the presence of protective silicide phases, which enhanced both mechanical and chemical stability in corrosive slurry environments. The complexity of the NAB microstructure, combined with the susceptibility of certain phases to selective phase attack, makes it essential to minimise the presence of vulnerable phases and to understand how microstructural characteristics influence performance under relevant service conditions.

2.3. Cavitation erosion-corrosion

This section reviews research on the cavitation erosion-corrosion performance of NAB in sulphide-polluted seawater, as well as examining the effects of rare earth additions, applied compressive stress, surface oxide film state (pre-conditioning), and manufacturing route including forged, cast and direct energy deposited materials. It also considers work on laser surface alloying of manganese aluminium bronze alloys.

As discussed above, the presence of sulphides in seawater and other chloride-containing environments can significantly compromise the integrity of corrosion product films on copper-based alloys, including NAB [3]. Elselstein et al. [16] support Meigh's observations regarding the synergistic interactions between sulphide and oxygen, which inhibit the formation of protective cuprous oxide films [3]. Their study showed localised corrosion rates of Cu-10Ni in aerated sulphide-polluted seawater were 155 times greater than in aerated unpolluted seawater. Similarly, Hazra et al. [45] report severe selective phase corrosion (SPC) and pitting corrosion of NAB exposed to sulphide-polluted seawater, while Li et al. [46] found enhanced erosion rates of Al brass and Cu-Ni alloys due to sulphide-induced embrittlement. More recently, Song et al. [19] investigated the effect of sodium sulphide (Na_2S) concentration on the corrosion and cavitation erosion performance of cast NAB in 3.5 wt% NaCl solution. Sulphide-polluted solutions were prepared with Na_2S concentrations of 20, 50, 100 and 200 ppm. In unpolluted NaCl solution, the mechanical erosion dominated the degradation process. However, under cavitation erosion-corrosion conditions in the polluted sulphide solutions, the synergistic term ΔE_C became the dominant contributor to mass loss, particularly at sulphide concentrations above 50 ppm. At 200 ppm concentration levels the erosion-corrosion rates were five times higher than those observed at 0 ppm.

Rare earth element additions [7] such as cerium (Ce), samarium (Sm) and ytterbium (Yb) have been shown to improve the cavitation erosion resistance of NAB in 3.5 wt% NaCl solution. These improvements arise from enhanced mechanical properties and microstructure refinement, particularly through the reduction in the size of κ_I and κ_{II} intermetallic phases. This refinement was reported to inhibit crack propagation at the phase boundaries between α and κ phases, thereby significantly reducing cavitation-induced erosion damage. In addition to mechanical improvements, the corrosion resistance of the NAB alloy also increased with the addition of Ce or Sm or Yb. However, the protective effect diminished over prolonged immersion, leading to increased levels of cavitation erosion. Notably, the addition of Yb reduced the maximum depth of erosion by 33% compared to untreated as-cast NAB.

The presence and stability of oxide surface films are key factors influencing the cavitation erosion-corrosion performance of as-cast NAB alloy [4]. Another important factor is whether cavitation is applied continuously or in a start-stop cycle, as this transient interruption can affect film breakdown and repassivation behaviour. This study uses both pulsed and continuous ultrasonic cavitation in accordance with ASTM G32. Initially, samples were assumed to have air-formed oxide films. The synergy component (S) of the total loss (T) was significantly affected by cavitation mode. Under continuous cavitation, the S accounted for 51.7% of the total loss, whereas in pulsed mode, it dropped to 25.6%. The reduced synergy in pulsed cavitation was attributed to rapid healing of the oxide film during cavitation-free intervals, which resisted erosion and lower mass loss. Basumatary and Wood [28] further explored the role of oxide films by comparing cast NAB (NES 747 Part 2) samples with air-formed films (after two weeks) and water-formed (after three months in 3.5 wt% NaCl). A synergy was reported of 70% for water-formed oxide films, compared to about 19% for the air-formed films. The

thicker oxide layer (between 1.0 and 1.2 μm), composed mainly of Al_2O_3 and Cu_2O, formed during prolonged immersion, provided partial protection but also contributed to selective phase corrosion, particularly at κ_{III} phases and $\alpha+\kappa_{III}$ eutectoid boundaries.

The type of oxide film present strongly influences the synergistic effects for cast NAB (NES 747) [44]. In the study, two types of surface films were examined: air-formed produced after two months of exposure, and anodic oxide films generated via electrochemical polarisation in 3.5 wt% NaCl solution. The anodically formed oxides films have a more electropositive open-circuit potential (OCP) and lower corrosion current density (i_{corr}), indicating better corrosion resistance. However, after cavitation exposure, the air-formed oxide sample show better cavitation erosion-corrosion resistance. Interestingly, the synergy value for the anodic oxide film was appropriately three times higher than that of the air-formed film, suggesting that the protective oxide layer may be more susceptible to mechanical damage under cavitation.

The effect of compressive stress [5] on cavitation erosion-corrosion performance of NAB alloy shows enhanced degradation attributed to an increase in increase in corrosion-induced erosion (ΔC_E), driven by stress-induced lattice distortion and accelerated selective phase corrosion. These effects also contributed to increased surface roughness, further exacerbating materials loss.

Influence of surface engineering techniques on NAB performance is given by Cheng Xu et al. [30] who examined the mechanical properties and cavitation erosion-corrosion behaviour of NAB alloys produced by directed energy deposition (DED) compared to conventional as-cast NAB alloys, in 3.5 wt% NaCl solution. The DED-produced NAB exhibited a finer and more uniform microstructure, with a significantly reduced volume fraction of κ-phases. These microstructural refinements led to a 27.8% increase in yield strength and 54.9% increase in elongation. Additionally, the DED-NAB alloy showed fewer high-angle grain boundaries (HAGBs), and $\sum 3$ twin boundaries, which contributed to a reduction in the synergistic effects between mechanical and corrosion degradation. Tang et al. [32] studied the cavitation erosion-corrosion behaviour of laser surface-alloyed manganese-nickel-aluminium bronze (MAB) in 3.5 wt% NaCl. A strong synergistic effect was reported, primarily driven by corrosion-induced erosion (ΔE_C), indicating that the surface modification significantly altered the degradation mechanism but the overall performance was improved. The cavitation erosion and corrosion behaviour of cast and forged NAB alloys have been studied in deionized water and artificial seawater by Ma [34]. Surprisingly, both material forms exhibited lower mass loss in seawater, indicating a negative synergy, where the combined effect of erosion and corrosion was less than the sum of the individual contributions. These findings align with previous work by the authors [42], which also reported negative synergy for NAB (NES 747 Part 2) under slurry erosion-corrosion. In those tests, a 3.5% NaCl solution containing 3% (wt./wt.) silica sand (135 or 235 μm) using jet velocities ranging from 3.1 to 6.7 m s^{-1}, producing E_k values between 0.02 and 0.41 μJ. Cavitation erosion-corrosion performance of friction stirred processing (FSP) of as-cast NAB in both distilled water and artificial seawater was studied by Li and Sun [37]. FSP was shown to refine and improve the uniformity of the microstructure, leading to enhanced cavitation erosion resistance in both environments. For the as-cast NAB, the dominant contributor to mass loss was pure cavitation erosion with minimal influence from corrosion. In contrast, the FSP-treated NAB exhibited a more pronounced synergistic effect between cavitation and corrosion, with a 30% reduction in erosion-corrosion rate compared to as-cast NAB.

Li et al. [25] conducted a fundamental study on the corrosion behaviour of NAB in 3.5 wt% NaCl solution under varying cavitation erosion durations. Their work employed electrochemical noise (EN), scanning Kelvin probe force microscopy (SKPFM) and detailed surface morphology analysis to characterise the evolving damage processes (corrosion and surface damage mechanisms). Correlations between microstructure and cavitation erosion behaviour of NAB (assumed to be as-cast) in simulated seawater (2.4 wt% NaCl solution) were investigated by Zhang et al. [33]. The synergistic effect between erosion and corrosion accounted for 41.4% of the total mass loss, primarily due to the surface roughening and the accelerated crack propagation facilitated by corrosion.

Table 3 summarises the cavitation-erosion performance of NAB as reported in the literature. Most treatments of as-cast NAB (addition of Yb and FSP processing) appear to reduce loss rates by roughly 30%. DED-NAB showed the largest reductions at 75%. LSA MAB reduced mass loss by a factor of 9.8 compared to the untreated MAB. However, NAB with anodic and seawater filmed oxide layers yield 3 to 16.5 times higher loss rates compared to air filmed NAB.

2.3.1. *Microstructure-performance interactions during cavitation erosion-corrosion*

This section examines the interactions between microstructure and performance under cavitation erosion-corrosion. Heat-treated NAB alloys conforming to NES 747 are studied in Ref. [28], and were exposed to 3.5% NaCl solution and experienced selective phase attack, mainly at the κ_{III}-phases and the $\alpha+\kappa_{III}$ eutectoid phase boundaries. Both air-formed and water-formed oxide films on cavitated surface exhibited similar wear mechanisms. Initial degradation consistently occurred at the $\alpha+\kappa_{III}$ eutectoid boundaries, where corrosion penetrated 20–50 μm beneath the surface with larger cracks propagated deeper into the substrate along these boundaries. Regions rich in lamellar κ_{III} phases were shown to be most susceptible to wear, crack initiation and propagation.

The presence of sulphide in the environment intensifies selective phase corrosion in as-cast NAB alloys by aggressively degrading the β′-phases and eutectoid microstructure ($\alpha+\kappa_{III}$). This degradation weakens phase boundary cohesion and promotes a brittle fracture mode, greatly enhancing overall mass loss [19]. Incorporating rare earth elements into NAB [7], improved mechanical properties and refined the microstructure, particularly by reducing the size of κ_I and κ_{II}

Table 3
Cavitation erosion-corrosion performance.

Reference/ data number	Test type	Materials	Erosion-corrosion performance
[2] same as [19] DN1	ASTM G32	As-cast NAB	At 200 ppm sulphide levels loss rates are 5 times those at 0 ppm
[7] DN2	ASTM G32	Rare earth additions	Addition of Yb reduced MDE (depth) by 33% vs as cast NAB
[28] DN12	ASTM G32	Cast NAB NES 747	16.5 times increase in mass loss with a three-month formed water filmed oxide layer compared to air filmed oxide layer.
[44] DN12	ASTM G32	Cast NAB NES 747	Three times in mass loss with an anodic formed oxide layer compared to air filmed oxide layer.
[5] DN4	ASTM G32	As cast NAB	Compressive stresses gave 1.74 times greater damage compared to the unstressed condition
[30] DN15	ASTM G32	DED NAB	DED-NAB reduced the mass loss rate by 74.8% compared to as-cast.
[32] DN17	ASTM G32	Laser surface-alloyed manganese-nickel-aluminium bronze (MAB)	LSA MAB reduced mass loss by 9.8 times compared to the untreated MAB.
[34] DN20	ASTM G32	Cast and forged NAB	Both negative synergy in artificial seawater.
[37] DN23	Vibratory horn not to G32	FSP NAB	FSP offered 30% reduction in erosion-corrosion rate compared to as cast NAB.

intermetallic phases. This refinement inhibited crack propagation at the phase boundaries between α and κ phases, thereby significantly reducing cavitation-induced erosion damage. Under tensile stress, [5], selective phase corrosion of the eutectoid $\alpha+\kappa_{III}$ becomes more severe which enhances damage rates. In contrast, compressive stresses enhanced corrosion-induced erosion (ΔC_E), initiating lattice distortion and accelerated selective phase corrosion. In Ref. [25], and consistent with many studies, galvanic corrosion between the α- and the κ-phases was seen to promote corrosion along the boundary of the α/κ phase. Over prolonged exposure, the extent κ-phase stripping and selective phase corrosion diminished, suggesting a dynamic evolution of corrosion behaviour. Although the hard κ-phase had a higher resistance to cavitation compared with the α-phase, it often acted as the cathode while α-phase often acted as the anode, leading to accelerated corrosion of the α-phase when both were in contact. Therefore, the damage to the κ-phase was less severe than that observed for the α-phase. Cracks preferentially initiated along the α/κ phase boundaries due to stress concentrations and selective phase corrosion. Smaller κ-phases were more prone to detachment under cavitation conditions. Analysis by Ref. [33] also revealed micro-cracks initiate preferentially at the α/κ boundaries. These cracks are short but prone to lateral expansion, driven by the uniform distribution of κ_{IV}-phases within the α-phase. Ma et al. [34] compared forged and as-cast NAB. with the as-cast containing a large amount of α-phase and a small amount of β phase, whereas the foraged had the opposite phase distribution, with refined grain sizes across all phases. The forged NAB had better mechanical properties, such as yield strength, hardness and toughness. Cavitation of the as-cast NAB led to partial transformation of the α-phase into β phase on the surface. The thermal effects of cavitation enhanced surface oxidation of both NAB variants in the study, inducing dense preventing local melting and protected the soft α-phase from cavitation damage. However, it should be noted that the tests were conducted on as-cast NAB, and performance may have been improved had heat treatment been applied to remove the remove β phase prior to testing, as recommended in NES 747.

Direct Energy Deposition of NAB was shown to significantly refine the alloy's microstructure, producing a more uniform and finer grain structure in Ref. [30]. This refinement reduced the volume fraction of κ phases, which in turn enhanced mechanical performance. Specifically, the yield strength increased by 28% and elongation improved by 55%. The DED-processed NAB alloy also exhibited fewer high-angle grain boundaries and twin boundaries, which diminished the synergistic interaction between corrosion and mechanical wear, leading to improved overall durability.

Under pipe flow conditions, chromium additions to NAB [24] does not change the types of precipitated phases present in the alloy. However, chromium preferentially entered the κ-phase and partially solubilized into the matrix. This dual incorporation increased the hardness of both the κ-phase and the matrix. More importantly, the chromium addition reduced the potential difference between the κ-phase and the matrix, thus reducing the micro-galvanic corrosion between these regions. As a result, the alloy exhibited a 20% improvement in erosion-corrosion resistance at flow velocities of 3 m s^{-1}.

2.3.2. Performance of related marine materials and coatings under cavitation erosion corrosion

Studies beyond NABs and cupro-nickels have explored alternative materials and coatings for erosion-corrosion resistance. Al-Fadhli [47] investigated the erosion–corrosion behaviour of high velocity oxy-fuel (HVOF) thermally sprayed Inconel-625 coatings on various metallic substrates. The coating applied to a composite surface of stainless steel and carbon steel (welded together) experienced a greater degree of weight loss. Microscopic examination of the fracture surfaces revealed that metal removal was concentrated around the unmelted and the semi-melted particles within the deposited layer. Brownlie and Hodgkiess [48] studied the slurry erosion-corrosion behaviour of engineering materials used in the geothermal industry. Their findings showed that both super austenitic (UNS S31254) and Inconel 625 (UNS N06625) exhibited excellent erosion-corrosion resistance, with Inconel 625 demonstrating the greatest resistance to high angle corrosive wear.

The resistance to corrosion and cavitation erosion of cold metal transfer (CMT) of Inconel 625 and Hastelloy C-276 coatings, both nickel-based alloys, applied to 304 stainless steel substrates have been studied in 3.5 wt% NaCl solutions by Zhao et al. [22]. The Inconel 625 coating featured a γ-phase matrix with MC-type carbide precipitates, predominantly niobium carbide (NbC), while the Hastelloy C-276 coating had a γ-phase matrix and molybdenum-rich P phase (orthorhombic, intermetallic) and a topologically close-packed phase. Both coatings demonstrated superior corrosion and cavitation erosion resistance of the coatings compared to 304 stainless steel substrates. Overall, Hastelloy C-276 outperformed Inconel 625 as evidenced by its higher polarisation resistance and lower mean depth erosion rate, measured at 1.3 ± 0.15 μm h^{-1}. These results show the effectiveness of CMT-applied nickel--based alloy coatings in enhancing surface durability in chloride-rich environments, with Hastelloy offering particularly robust protection.

2.4. Fluid-flow

2.4.1. Pipe-flow

As suggested by Roberge [11] aluminium bronzes have a relatively low design velocity for pipe flow applications, typically under 2.7 m s^{-1}. Therefore, erosion-corrosion test conducted under pipe flow should carefully consider this velocity threshold when setting experimental parameters [11].

Wang et al. [24] reported the effect of chromium addition on the microstructure, mechanical properties and pipe-flow erosion-corrosion behaviour of NAB alloys. Chromium incorporation resulted in a 20% improvement in erosion-corrosion resistance compared to the unmodified alloy at flow rates of 3 m s^{-1}. Additionally, the corrosion product film formed on the surface contained Cr_2O_3 and Cr^{3+} species, which contributed to a denser and more protective oxide layer, further enhancing the corrosion resistance. Wang et al. [27] studied the impact of pre-soaking NAB alloy in artificial seawater for 0, 14, or 30 days prior to pipe flow erosion-corrosion testing. After 30 days immersion, a multi-layered passive film formed on the NAB surface, consisted of: an outer loose CuO layer; a middle dense layer of Cu_2O enriched with Fe, Ni, and Al; and a denser inner Cu_2O film contained a 10 nm thick layer Al_2O_3 layer adjacent to the substrate. This complex oxide structure significantly improved corrosion resistance, resulting in an approximate 71% reduction in corrosion rate at a flow velocity of 3 m s^{-1} compared with the unsoaked samples. In a separate study, Wang et al. [36] investigated the effects of hot extrusion on the microstructural evolution and erosion-corrosion behaviour of NAB alloy (Cu-9Al-4.5Ni-4Fe-1Mn, wt.%) under pipe-flow velocities between 0 and 3 m s^{-1}. Hot extrusion refined the microstructure disrupted layered structures and promoted spheroidization, leading to a more homogenous phase distribution. These microstructural changes led to improved mechanical behaviour (hardness, strength, and elongation) and higher resistance to both corrosion and erosion-corrosion compared to as-cast NAB.

2.4.2. Jet impingement

Cupro-nickels, along with NAB, are widely used in marine and desalination plant applications, with components such as valves, pumps, pipes, heat exchangers and propulsors commonly manufactured from these alloys. For this reason, recent research into cupro-nickels is included in this review. The erosion-corrosion behaviour of a Cu-10Ni-base alloy and a higher-strength (HS) Cu-Ni alloy under short-term liquid-impingement in 3.5% NaCl solution at ambient temperature has been studied [39]. This study revealed a complex interlay pure corrosion, mechanical erosion and synergy interactions. Erosion damage was primarily associated with cavitation effects in the directly impinged and closely adjacent regions, while electrochemical corrosion was linked to

the formation and breakdown of surface corrosion product films. For the Cu-10Ni alloy, substantial synergy contributions were observed, particularly corrosion-induced erosion (ΔE_c), where mechanical damage from cavitation facilitated further corrosion degradation at erosion pits. In contrast, the high strength Cu/Ni alloy exhibited synergistic mechanisms associated with micro-roughening due to non-uniform surface films and corrosion at second-phase precipitate particles. Interestingly, while the high strength Cu/Ni alloy showed lower total erosion-corrosion material loss, it was less resistant to pure corrosion than the Cu/10Ni alloy. The authors noted that alloying and microstructural modifications aimed at improving mechanical strength can inadvertently reduce corrosion resistance, highlighting the complexities of erosion-corrosion behaviour.

3. Mapping synergy

Quantification of E, C, T and S in the reviewed papers, where these parameters were measured, was carried out using mass loss data or electrochemical measurements followed by Faradaic conversion. Typically, three tests are conducted:

- C (corrosion-only component) obtained from static immersion in a sodium chloride solution, with corrosion current measured electrochemically. In some studies, *in situ* electrochemical measurements to capture $C+\Delta C$, where ΔC accounts for time-dependent changes in corrosion rate during erosion-corrosion;
- E (pure erosion) determined using distilled water to limit electrochemical effects, and;
- T (total material loss under erosion-corrosion) measured during simultaneous erosion and exposure to sodium chloride solution.

The synergistic component S is typically quantified using: $S = T-(E+C)$ or $\Delta E = T-(E+C+\Delta C)$ and where $T = \Delta E + \Delta C$ in time dependent approaches.

These relationships allow decomposition of total material loss into mechanical, electrochemical, and synergistic contributions.

Wood and Hutton [49] demonstrated that mapping the ratio of synergy to corrosion (S/C) against erosion to corrosion (E/C) provides a powerful framework to evaluating the degree of synergism under various erosion and corrosion conditions and for various materials. The analysis revealed that for the materials classified within medium and high S/C groups, the data follow a linear relationship on a log-log scale, allowing predictive modelling of synergistic wear rates. The best-fit lines derived for each group closely matched experimental measured wear rates for both cavitation erosion and slurry erosion-corrosion tests, validating the approach. In the medium S/C group, the synergistic mechanism may reach a maximum when erosion dominates and remains corrosion low, resulting in a maximum magnification (M) of 2 ($M = T/(E+C)$). In the high S/C group, the maximum magnification reaches $M = 2.7$ when $E/C \approx 1$, indicating a balanced contribution from erosion and corrosion. The authors attribute this magnification to the exposure of fresh surfaces during erosion, which are not immediately passivated by corrosion products, therefore accelerating corrosion rates. The largest magnification reported is 3.7 observed for 0.2 wt% phosphorus grey cast iron tested at 50 °C in 3% NaCl solution under vibratory cavitation erosion-corrosion [50].

Building on this framework, a new map has been constructed below using S/C *vs.* E/C data extracted from the reviewed literature in this paper, where synergy values were explicitly quantified. This data is tabulated in Table 4 and plotted in Fig. 5, the presence of 200 ppm sulphides in the test solution produced an extremely synergistic response (fitted Equation (3)), with magnification factor of $M = 8.7$, *i.e.*, $T = 8.7(E+C)$. This highlights the severe impact of sulphide contamination on erosion-corrosion performance and demonstrates the utility of the S/C *vs.* E/C mapping approach for predicting erosion-corrosion degradation in complex environments. Other very highly

Table 4
Data from the reviewed literature that reported quantifying synergy (S) or its components (ΔE_C and/or ΔC_E) alongside T, E and C. These points are plotted on Fig. 4.

Material/test	Ref.	Condition	E/C	S/C	$M = T/(E+C)$
CNAB/cav/3.5% NaCl/no stress	[2]	s0	55.9	33.4	1.59
CNAB/cav/3.5% NaCl/20 sulphur	[2]	s20	121.5	138.9	2.13
CNAB/cav/3.5% NaCl/50 sulphur	[2]	s50	138.0	460.8	4.32
CNAB/cav/3.5% NaCl/100 sulphur	[2]	s100	151.9	718.3	5.70
CNAB/cav/3.5% NaCl/200 sulphur	[2]	s200	54.2	425.7	8.71
CNAB/cav/3.5% NaCl/oxide	[4]	Surface oxides	37.4	41.0	2.07
CNAB/cav/3.5% NaCl/0 stress	[5]	Stress 0 MPa	68.2	33.7	1.49
CNAB/cav/3.5% NaCl/60 stress	[5]	stress 60 MPa	72.0	54.8	1.76
CNAB/cav/3.5% NaCl/120 stress	[5]	stress 120 MPa	74.0	103.8	2.39
CNAB 747/cav/3.5% NaCl/air oxide	[44]	Air formed oxide	555.6	77.8	1.14
CNAB 747/cav/3.5% NaCl/anodic film	[44]	Anodic formed oxide	6454.5	4000.0	1.62
CNAB 747/cav/3.5% NaCl/air oxide	[28]	air formed oxide after 1 week	5.0	1.4	1.23
CNAB 747/cav/3.5% NaCl/water film	[28]	Oxide formed after immersion in water for 3 months	367.0	851.0	3.31
90/10 Cu/Ni/jet impact/3.5% NaCl	[39]	Velocity of 2.4 m s^{-1}	2.50	1.92	0.77
90/10 Cu/Ni/jet impact/3.5% NaCl	[39]	Velocity of 4.5 m s^{-1}	2.69	0.92	0.34
90/10 Cu/Ni/jet impact/3.5% NaCl	[39]	Velocity of 4.5 m s^{-1}	3.33	1.22	0.37
90/10 Cu/Ni/jet impact/3.5% NaCl	[39]	Velocity of 17 m s^{-1}	1.82	6.27	3.45
90/10 Cu/Ni/jet	[39]	Velocity of 86 m s^{-1}	1.35	3.59	2.66

(*continued on next page*)

Table 4 (*continued*)

Material/test	Ref.	Condition	E/C	S/C	$M = T/(E + C)$
impact/ 3.5% NaCl					
HS Cu/Ni/jet impact/ 3.5% NaCl	[39] HS Cu/Ni	Velocity of 2.4 m s^{-1}	0.0056	0.67	1.66
HS Cu/Ni/jet impact/ 3.5% NaCl	[39]	Velocity of 4.5 m s^{-1}	0.0071	3.29	4.26
HS Cu/Ni/jet impact/ 3.5% NaCl	[39]	Velocity of 4.5 m s^{-1}	0.0056	1.22	2.21
HS Cu/Ni/jet impact/ 3.5% NaCl	[39]	Velocity of 17 m s^{-1}	0.385	0.5	1.39
HS Cu/Ni/jet impact/ 3.5% NaCl	[39]	Velocity of 86 m s^{-1}	0.435	1.17	1.82
CMAB/cav/ 3.5% NaCl	[32]	As cast MAB	414.90	31.94	1.08
MAB-LSM/ cav/3.5% NaCl	[32]	MAB-LSM	91.47	34.29	1.37
MAB-Al-8/ cav/3.5% NaCl	[32]	MAB-Al-8	27.5	68.58	3.41
CNAB/cav/ 2.4% NaCl	[33]	Cast Ni-Al bronze	50.17	36.33	1.71
CNAB/pipe-flow/art s/w	[36]	As cast NAB	38.57	5.19	1.13
FSP-NAB/ pipe-flow/ art s/w	[36]	FSP-NAB	17.76	24.66	2.31
CNAB/cav/ art s/w	[37]	As cast NAB	55.81	12.84	1.23
CNAB/cav/ art s/w	[37]	As cast NAB	56.89	14.43	1.25
CNAB/cav/ art s/w	[37]	As cast NAB	20.86	12.33	1.56
CNAB/cav/ art s/w	[37]	As cast NAB	3.54	10.75	3.37
CNAB/cav/ art s/w	[37]	As cast NAB	1.36	6.74	3.86
CNAB/cav/ art s/w	[37]	As cast NAB	37.81	17.56	1.45
CNAB/cav/ 3.5% NaCl	[30] cnab	As cast NAB	0.83	5.31	3.91
DEDNAB/ cav/3.5% NaCl	[30] dnab	Direct energy NAB	4.02	3.78	1.75
CGI/cav/3% NaCl 50C	[49]	Grey cast iron (point 14)	2	100	100
	[49]	High	0.0	0.1	0.1
Mixed cons	[49]	High	1000.0	635.0	635.0
Mixed cons	[49]	medium	0.0	0.0	0.0
Mixed cons	[49]	medium	1000.0	1001.0	1001.0

Where s0, s20, s50, s100, s200 are Na_2S concentrations of 20, 50, 100 and 200 ppm, **Mixed cons** (*i.e.*, mixed conditions) are trend lines using data from slurry, hydrodynamic and ultrasonic cavitation tests.

synergistic combinations are cavitation on cast NAB (747) after three months immersion in salt water, some jet impingement conditions on cupro-nickel (90/10), cavitation erosion-corrosion of MAB-Al-8, cast NAB (unheated treated) in artificial seawater and one report of cast NAB under ASTM cavitation conditions. The least synergistic appears related to the environment such as lower NaCl concentration or artificial seawater under cavitation and flow conditions as well as the use of as-cast manganese aluminium bronze and LSM surfaced treated MAB.

The extremely synergistic line group is given by a best fit line below:

$$\frac{S}{C} = \exp\left[\left\{0.51 \ln\left(\frac{E}{C}\right) + 3.892\right\}\right] \quad (3)$$

It is also interesting to note that high levels of synergy are created for E/C ratios above unity. This indicated that synergy is possible and maybe linked to dominant mechanical processes.

4. Synergistic mechanisms

As discussed in the reviewed literature, synergy in erosion-corrosion appears closely linked to the distribution of to κ-phase and β phase, galvanic coupling and work hardening effects. The positive synergy mechanisms identified across studies are summarised in Table 5. These mechanisms typical involve corrosion-induced erosion, where mechanical damage exposes fresh surfaces that are not immediately passivated, accelerating corrosion and increasing total material loss. Conversely, negative synergy is coupled with a zero ΔC_E inferred a negative ΔE_C solely responsible for reducing T to levels below $E + C$.

Mechanisms proposed for this negative are listed in Table 6. For NAB materials, the most likely cause of negative synergy by ΔE_C is the presence of loose surface films and/or corroded microstructures. These features can alter the contact mechanics between the impacting sand particles and the NAB surface, reducing mechanical erosion (E). Such filmed surfaces have increased compliance to resist impacts by cavitation bubble microjets and solid particle. Thermal effects from cavitation have also been cited as modifying corrosion mechanism by promoting the formation of dense and adherent oxide films. These films act as a barrier to further erosion damage, thereby reducing the overall material loss through a negative ΔE_C effect.

From Table 7, the damage patterns under cavitation erosion-corrosion show highly complex interactions between mechanical processes and microstructure that evolve over time and are difficult to summarise generically. In certain environments, individual phases are preferentially attacked by erosion-corrosion mechanisms, whereas in others such as sulphide containing environments, the damage appears to be largely independent of microstructure [2]. This behaviour relates to highly synergistic performance (Fig. 4), where the mechanical integrity of the surface is severely compromised. Other studies reporting strong synergy [26,51] show pronounced selective phase attack at α-κ phase boundaries, leaving κ_I globules and κ_{III} lamellar phases exposed and reduced surface integrity through anodic film formation.

Several researchers have attempted to identify the microstructural phases most vulnerable that might be contributing the synergy, often linking these phases to evidence of brittle fracture or surface cracking. Studies examining the effects of compressive stress [5] report the formation of microcavities and pitting on the surface, as well as cracks. Under non-ASTM cavitation test conditions [3], micro ploughing, plastic lipping and pitting are active degradation mechanisms. Li et al. [25] further show the vulnerability of the β phase to erosion. Common to many studies, selective phase corrosion at α-κ phase boundaries is a recurring observation [19], and this behaviour would be a driver of positive synergy by undermining the surface integrity and resistance to mechanical erosion processes, as seen in Table 5. The identification of corrosion films is less well established across the published literature, but their characteristics are important to interpreting negative synergy interactions, as shown on Table 7. In slurry cavitation-erosion tests reported in Ref. [36] shows corrosion products are formed on the surface, although synergy was not quantified. Other slurry erosion-corrosion studies [27,29] provide only low-quality images of the post-test surfaces, preventing detail assessment of erosion-corrosion mechanisms.

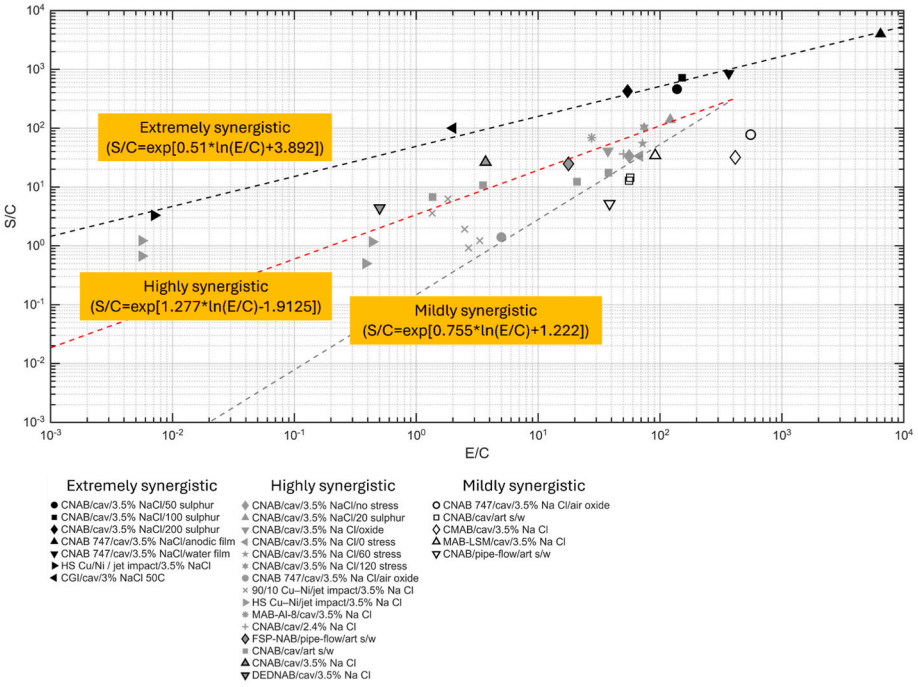

Fig. 5. S/C ratios plotted against E/C ratios for NAB.

Table 5
Positive synergy terms.

Positive synergistic mechanisms	
ΔE_C	ΔC_E
Preferential corrosion (selective phase corrosion, particularly at the κ_{III} phases and the $\alpha+\kappa_{III}$ eutectoid boundaries) of anodic phases, boundaries between phases that undermine the bonding of the harder phases. i.e., loss of both hard κ and β phases, alongside distortion of ductile α phase.	Increased flow assisted corrosion and stripping of surface oxide films.
The presence of sulphide and oxygen in the environment aggravates selective phase corrosion, particularly at the β' phase and eutectoid microstructure ($\alpha+\kappa_{III}$), weakening the phase boundary cohesion and promoting brittle fracture.	Slow repassivation rates enhance corrosion rates.
Depending on strain/residual stress levels and amount of strain hardening at the surface the damage can switch to brittle, cleavage-like fracture.	Enhancing oxygen mass transfer due to cavitation increases corrosion rates.
Corrosion accelerated crack growth.	Stress-induced lattice distortion and accelerated SPC due to compressive stresses.

Table 6
Negative synergy terms.

Negative synergistic mechanisms	
ΔE_C	ΔC_E
Increased work hardening due to corrosion mechanisms.	Thermal effects from cavitation have also been cited as modifying corrosion mechanism by promoting the formation of dense and adherent oxide films. These films act as a barrier to further erosion damage, thereby reducing the overall material loss.
Shot-peening effects from high velocity particle impacts.	
The formation of a soft or loosely adherent corrosion films.	
Crack tip blunting by lateral dissolution slowing crack propagation.	
Rapid growth of corrosion films which act as physical barriers to erosion.	

5. Conclusions

5.1. Summary of review

Recent studies of NAB erosion-corrosion and related alloys and coatings reveal a lack of consistency in experimental approaches and reported data. Researchers have studied a wide range of NAB variants, including as-cast (with some heat treated), powder metallurgy, friction stir welding, hot extrusion and shot peened, with some incorporating additions of rare earth elements or chromium. However, this diversity in alloy processing has made meaningful comparisons difficult. Most studies focus on air-filmed surfaces immediately after casting, with only a few investigating the role of surface films through pre-conditioning, such as two-week immersion. Even fewer studies follow the heat treatment protocols recommended in NES 747 Part 2, which aim to reduce the presence of the retained β-phase, known to compromise NAB corrosion performance. Moreover, researcher have largely overlooked the three-dimensional nature of the erosion-corrosion, which extends beyond the surface into subsurface microstructure. This omission limits the ability to correlate material performance with mechanical properties and synergy effects. As a result, the field lacks a reliable dataset, and no standardised protocol exists for testing or reporting erosion-corrosion behaviour. Establishing such a protocol is urgently needed to enable fair comparisons and informed material selection.

This review highlights the complex interplay between microstructure, electrochemical activity, and mechanical stress in governing the erosion-corrosion performance of NAB alloys. The dynamic interactions between microstructural evolution, phase stability, and surface film formation under mechanical action in saline environments can, under some circumstances, contribute to the developments of protective films rather than material degradation. However, meaningful comparison across published studies remains difficult. Much of the available

performance data is benchmarked against as-cast NAB rather than material heat-treated to the NES747 specification, and the lack of standardised test conditions further complicates interpretation. Most experiments are short-term and do not include surface conditioning, despite the fact that in service exposure is rarely continuous and typically involves stop-start operation, intermittent mechanical damage, and biofouling.

A direct comparison of cavitation erosion-corrosion and slurry erosion-corrosion effects on NAB microstructure was not possible based on the current published literature. Such a study would provide valuable insight and represents a promising direction for future research.

5.2. Concluding remarks

The NAB performance under slurry erosion-corrosion shows that peening, laser treatment, quenching treatments of as-cast NAB reduce material loss rates by 30% compared to as-cast NAB. Powder metallurgy shows more modest reduction of 11%. High strength manganese-silicon alloys and electroplated Ni-Al-Cu coatings applied to NAB yield the most significant reductions of 45% and up to 90%, respectively.

Under cavitation erosion-corrosion, additions of Yb and FSP processing of as-cast NAB reduce loss rates by around 30%. Direct Energy Deposition of-NAB gave the largest reduction of 75%. Laser treatments of MAB reduced mass loss by 9.8 times compared to the untreated MAB.

Anodic and seawater filmed oxide layers yield 3 to 16.5 times higher loss rates compared to air filmed NAB showing that conditioning and the type of surface layer on NAB is critical to understand along with subsurface selective phase corrosion that undermines the integrity of the material to resist mechanical aspects of erosion.

S/C plotted against E/C shows an extremely synergistic combinations of alloy-environment combinations.

Extremely low synergistic conditions where M is approximately 1 or below down to 0.3 are seen which are good material/environment combinations.

Negative synergy in a few tests (both slurry and cavitation erosion-corrosion) is seen and where strong surface films are generated.

Cavitation, flow and slurry erosion-corrosion activate similar degradation processes that target specific phases within the microstructure of NAB surfaces including loss of hard phases κ and β, the ductile response of alpha phases, silicide phases, size of α- and κ-phases, β-phase corrosion, α/κ phase boundaries corrosion, κ_{III} phase eroded, α anodic and κ cathodic.

The three-dimensional nature of the erosion-corrosion, which extends beyond the surface into subsurface microstructure, generally overlooked and should be included in future papers.

CRediT authorship contribution statement

Robert JK. Wood: Writing – original draft, Formal analysis, Data curation, Conceptualization. **Julian A. Wharton:** Writing – review & editing.

Declaration of competing interest

The authors declare that they have no known competing financial interests or personal relationships that could have appeared to influence the work reported in this paper.

Appendix

Table 7
The variation in initial microstructure of the materials and coatings tested and reported in this paper. Initial and the most relevant damaged surfaces where available are included. Listed by reference and data number (DN).

[19], DN 1
Cast NAB and MAB

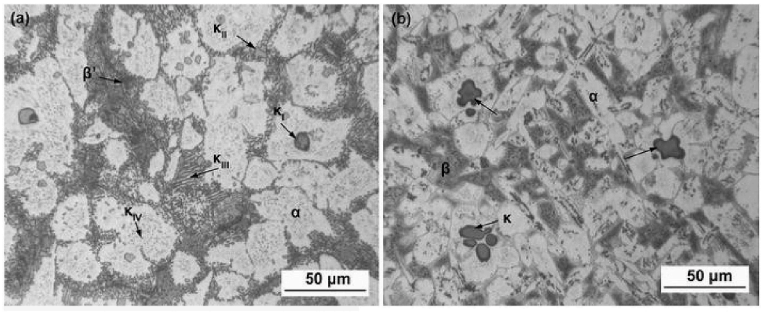

Optical microstructure of the cast NAB and MAB.

(*continued on next page*)

Table 7 (*continued*)

	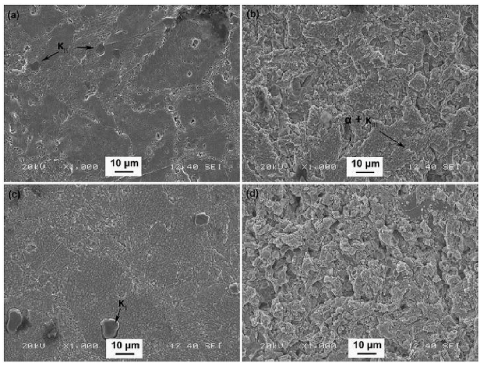 Surface morphologies of the cast NAB after cavitation erosion in (a, b) clean, (c, d) sulfide-polluted 3.5% NaCl solutions for different time: (a, c) 1 h; b, and (d) 3 h.	
[2] DN1 Cast NAB	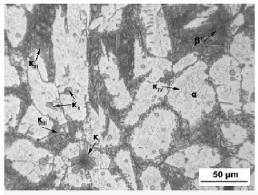 Optical microstructure of the cast NAB	
	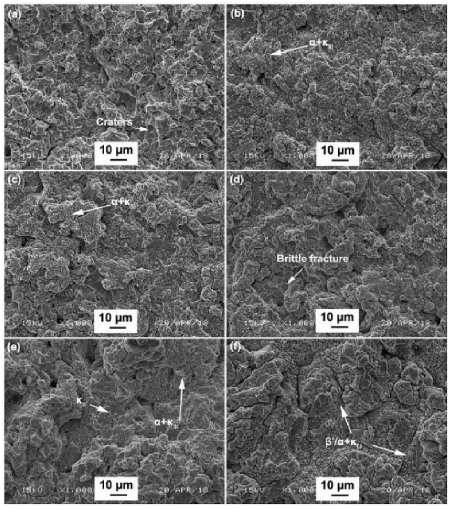 Surface morphologies of NAB after cavitation erosion for 5 h in **(a)** distilled water and 3.5% NaCl solutions with sulphide concentrations **(b)** 0 ppm, **(c)** 20 ppm, **(d)** 50 ppm, **(e)** 100 ppm, **(f)** 200 ppm.	
[7], DN2 Cast NAB	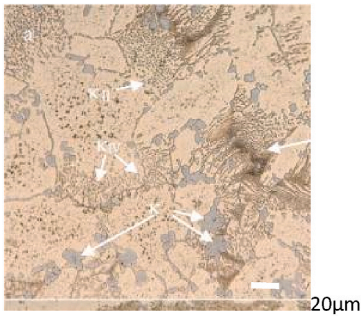 NAB alloy	

(*continued on next page*)

Table 7 (*continued*)

	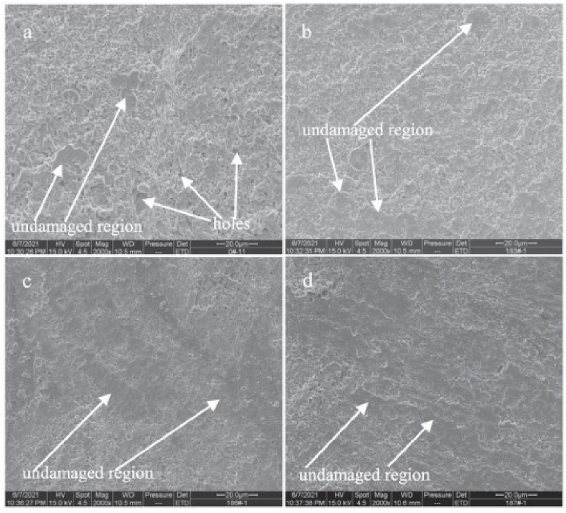 Front SEM images of NAB alloys after cavitation erosion for 2 h in 3.5% NaCl solution and in the case of without immersion (0 day), **(a)** NAB alloy, **(b)** NAB-Ce alloy, **(c)** NAB-Sm alloy, and **(d)** NAB-Yb alloy.
[4], DN3 [5], DN4 Cast NAB	N/A
	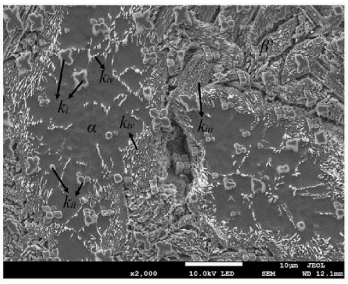 Microstructures of an as-cast NAB alloy.
	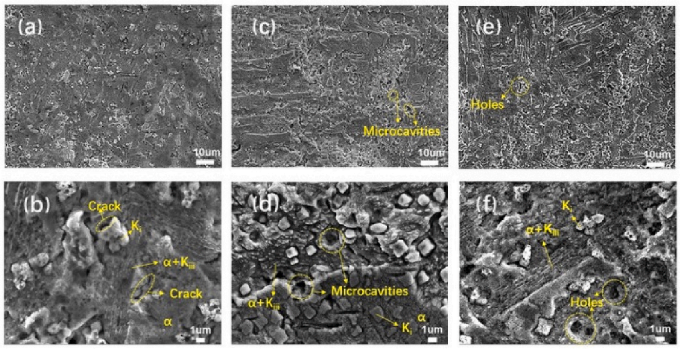 Surface micrographs of the NAB alloy with **(a, b)** 0 MPa, **(c, d)** 60 MPa and **(e, f)** 120 MPa compressive stress after cavitation corroded for 3 h in 3.5 wt% NaCl solution.
[6] DN5	N/A

(*continued on next page*)

Table 7 (*continued*)

[23], DN6
Cast NAB and Friction stirred NAB

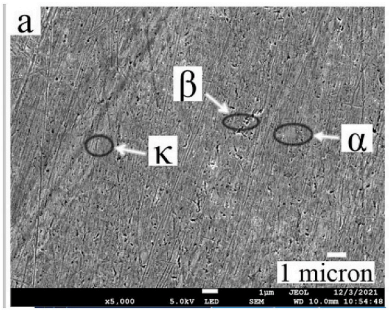

FE-SEM of as-cast NAB.

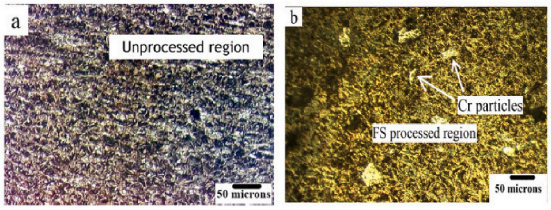

Optical micrographs of (**a**) the as-cast NAB and (**b**) FS-processed stir zone showing the distribution of particles.

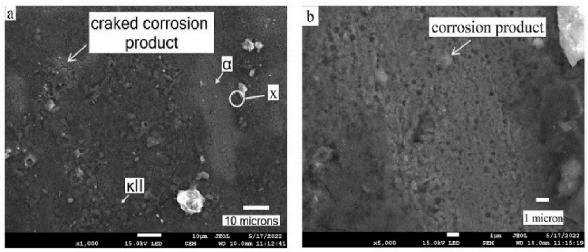

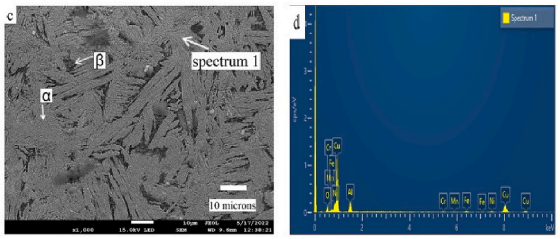

Scanning electron microscope morphology of slurry erosion-corrosion for **(a)** as-cast NAB at 30° (1000 ×), **(b)** magnified image at X (5000 ×), and for **(c)** FSPed composite at 30° (1000 ×), and **(d)** EDS image of spectrum 1.

[24], DN7&8
Cast NAB and Cast NAB-Cr

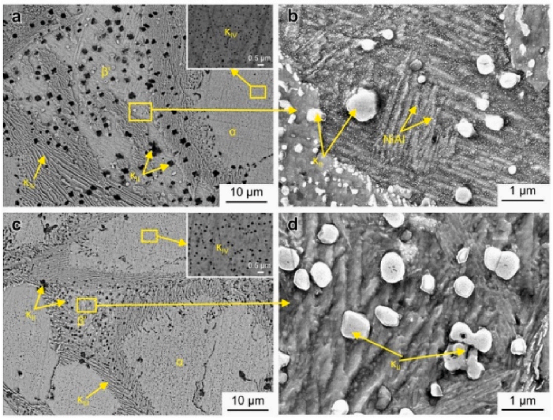

SEM images of microstructure of **(a**, **b)** Z alloy and **(c**, **d)** Z–Cr alloy.

(*continued on next page*)

Table 7 (*continued*)

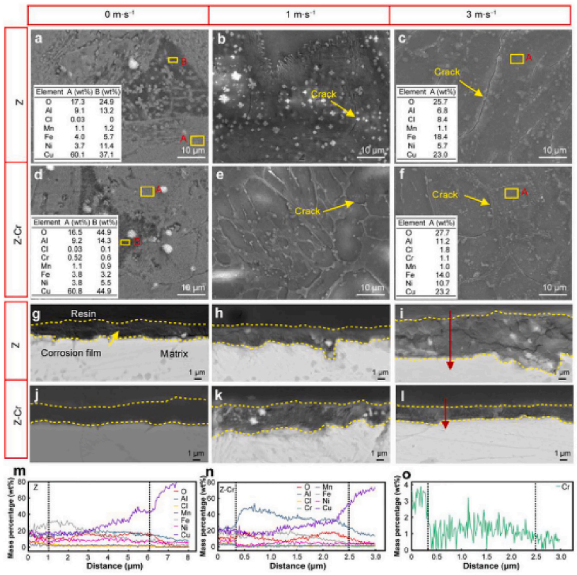

Fig. 6 Corrosion product film analysis of Z and Z–Cr samples after 21-days erosion in artificial seawater at different flow rates: a–f surface corrosion products; g–l cross-section corrosion films; m–o cross-section line sweeps of Z and Z–Cr alloys subjected to 3 $m \cdot s^{-1}$ erosion

[25], DN 9
Cast NAB

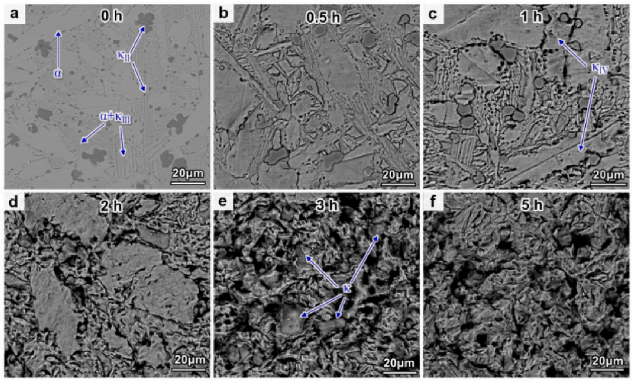

Surface morphologies of NAB after different CE times: (**a**) 0 h; (**b**) 0.5 h; (**c**) 1 h; (**d**) 2 h; (**e**) 3 h; and (**f**) 5 h.

[26], DN10
Cast NAB, Ni-Al-Cu electroplated coating, Ni-Al-Cu Coatings

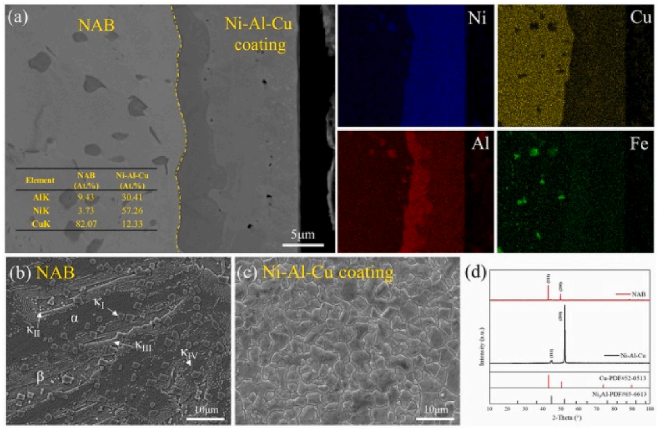

(a) BSE of cross-sectional morphology of the Ni-Al-Cu electroplated coating and the corresponding EDS mapping results, and SEM images for the microstructure of **(b)** NAB alloy and **(c)** Ni-Al-Cu coating with (d) the corresponding XRD patterns.

(*continued on next page*)

Table 7 (*continued*)

	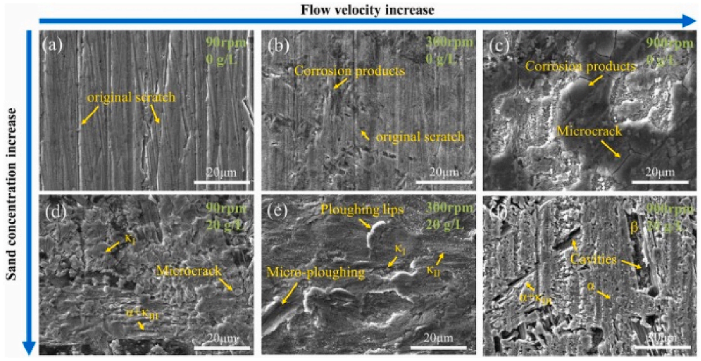 High magnification SEM micrograph of eroded surface of NAB alloy.
	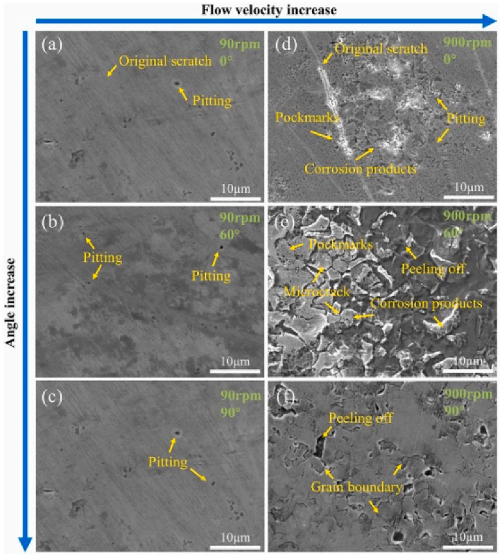 High magnification SEM micrograph of eroded surface of Ni-Al-Cu coating.
[41], DN0 Cast NAB and laser processed NAB	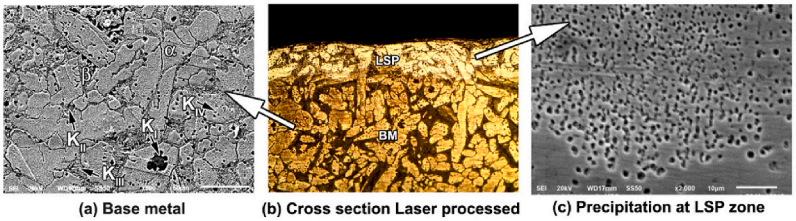 Microstructural features of as-cast and laser processed NAB.
	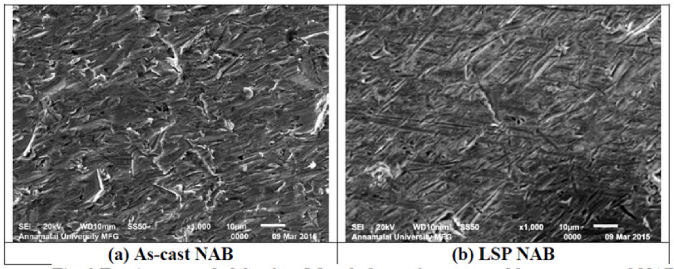 **Fig. 8 Erosion corroded Surface Morphology of as-cast and laser processed NAB**

(*continued on next page*)

Table 7 (*continued*)

[27], DN11
Cast NAB

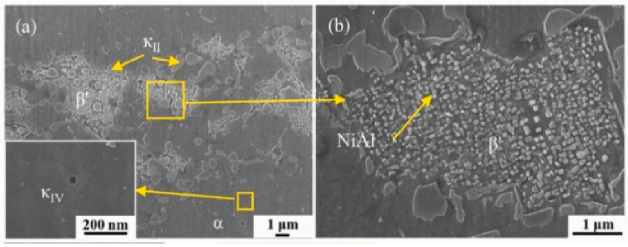

Microstructure of the as-prepared NAB alloy (PS-0): **(a)** SEM; **(b)** β′ phase high magnification SEM image.

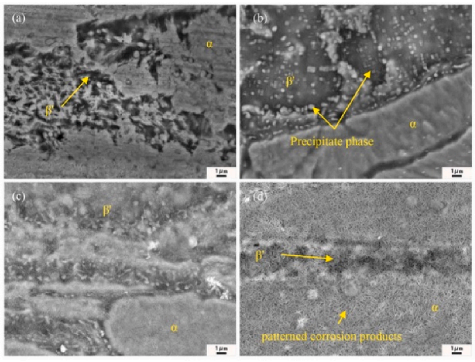

SEM images of surface films on NAB alloy samples after different static immersion times: **(a)** 1 d; **(b)** 7 d; **(c)** 14 d; and **(d)** 30 d.

[21,28,51] DN12
Cast NAB

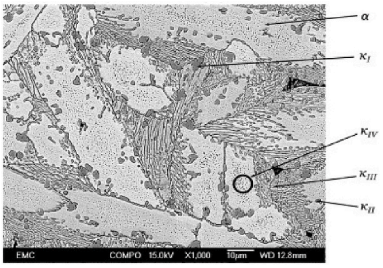

SEM backscattered electron image of the microstructural morphology of cast NAB.

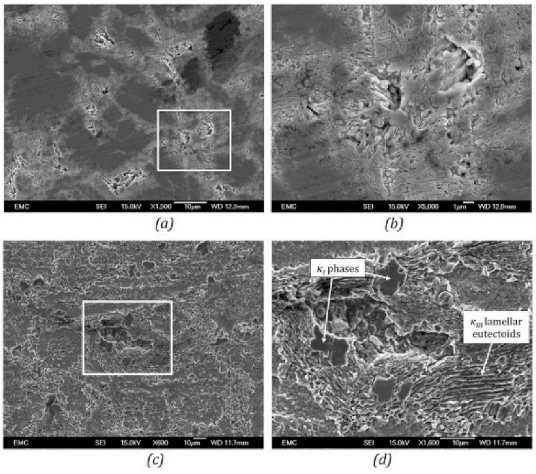

SEM compo/backscattered images of **(a)** small boundary erosion on air-formed filmed NAB in distilled water after 1 h; **(b)** shows the magnified image of the cavities of size 10-μm at the selected area in **(a)**; **(c)** SEM image of a 50-μm large cavity on the sample surface undergone cavitation erosion-corrosion in 3.5% NaCl solution after 1 h; and **(d)** the magnified image of a cavity in (c) showing selective phase attack at the α-κ phase boundaries leaving κ_I globules and κ_{III} lamellar phases exposed.

(*continued on next page*)

Table 7 (*continued*)

	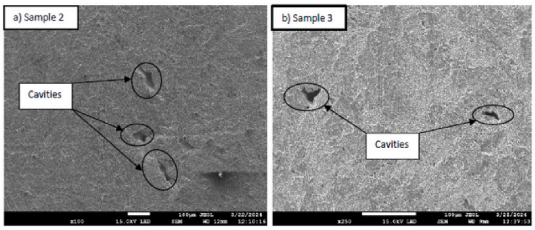 SEM image of **(a)** anodic filmed sample surface after 1 h of cavitation in 3.5% NaCl with cavities in the range of 65 μm-125 μm. **(b)** Sample surface after 1 h of cavitation in distilled water with cavities in the range of 30 μm-35 μm.
[26], DN12 Cast NAB 747	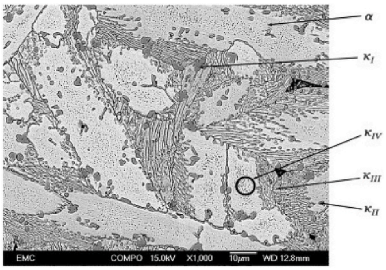 SEM backscattered electron image of the microstructural morphology of cast NAB.
	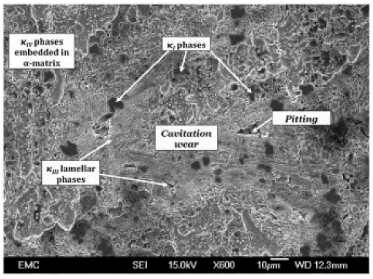 SEM image of the eroded surface of NAB sample with water-formed oxide film after combined cavitation erosion-corrosion test conducted in 3.5% NaCl solution for 1 h.
[39] DN 28 Cu-10Ni	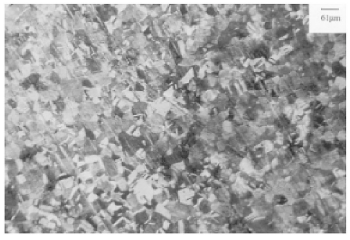 Etched metal structure beneath transparent coloured film on Cu-10Ni after 4 h impingement at 17 m s^{-1}.
[39] DN29 High Strength (HS) Cu-Ni	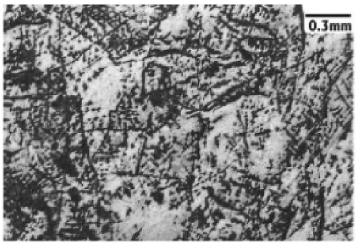 HS Cu/Ni after 4 h impingement at 4.5 m s^{-1}; central, directly-impinged zone.

(*continued on next page*)

Table 7 (*continued*)

[30], DN15 Cast NAB and Directed energy deposited DED NAB	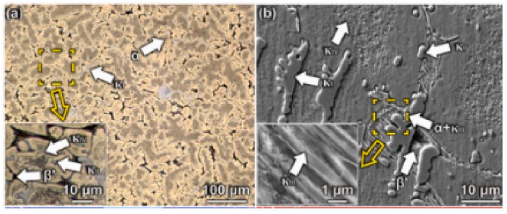 As cast NAB 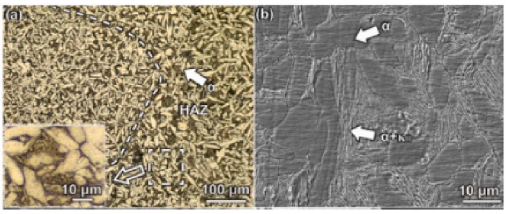 Directed energy deposited NAB 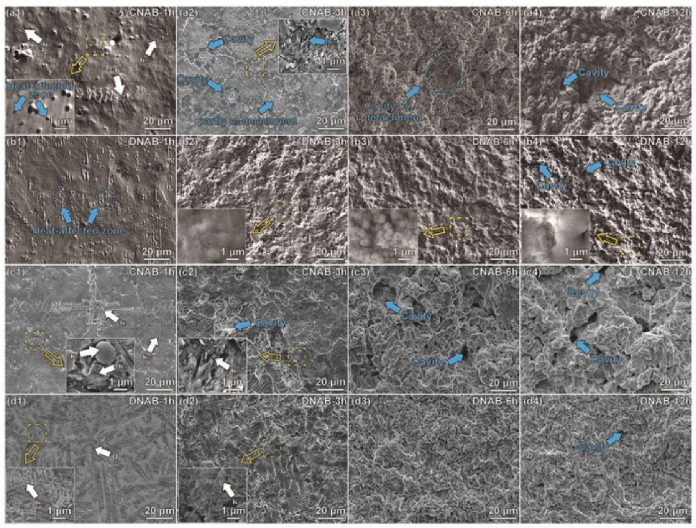

Surface morphologies of CNAB and DNAB after cavitation erosion in **(ai)**, **(bi)** distilled water and (ci), (di) 3.5 wt% NaCl solution; **(ai)**, **(ci)** CNAB, **(bi)**, and **(di)** DNAB (i = 1, 2, 3, 4).

(*continued on next page*)

Table 7 (*continued*)

[29] DN13&14 Cast NAB, Manganese-Silicon Brass	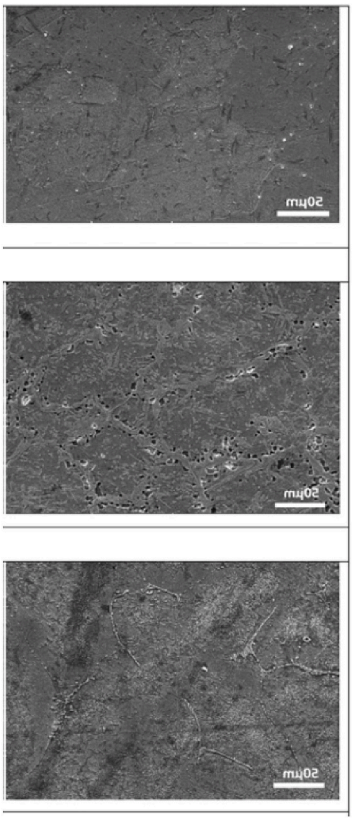

SEM micrographs of permanent mould case RB031, RB032 and NAB.

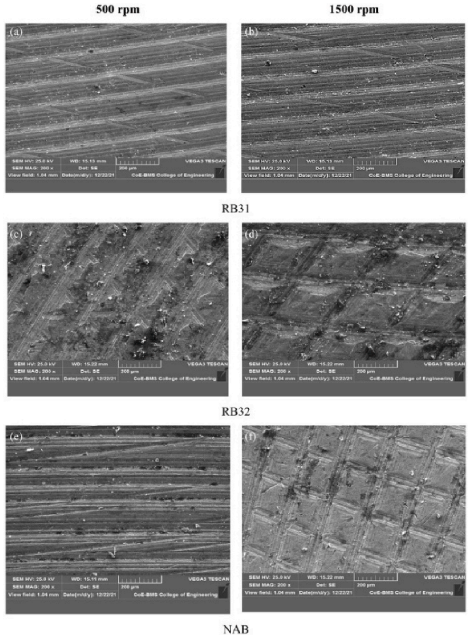

(a–f) SEM Micrographs of all the alloys RB031, RB032 and NAB (AB2) obtained after erosion-corrosion test.

(*continued on next page*)

Table 7 (*continued*)

[31], DN 16
Cast NAB and shot peened (SP) NAB

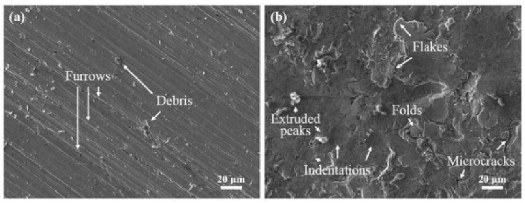

Surface morphologies of NAB before **(a)** and after **(b)** SP treatments.

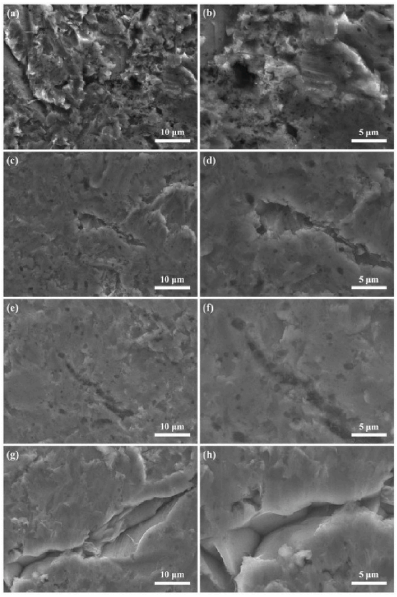

Variations of surface morphologies of **(a, b)** as-ground and SP-treated NAB with intensities of **(c, d)** 0.1 mmA, **(e, f)** 0.2 mmA, and **(g, h)** 0.2 + 0.1 mmA after E-C test for 60 min. Note mmA is linked shot-peen treatment.

[32], DN17
Cast MAB and laser surface melted MAB

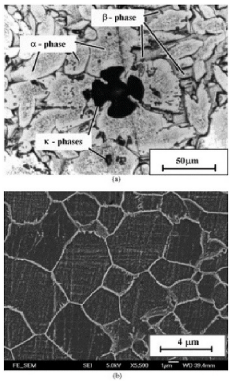

Microstructure of **(a)** as-received MAB (optical micrograph) and **(b)** laser surface-melted sample MAB-2-35 (SEM micrograph at a higher magnification).

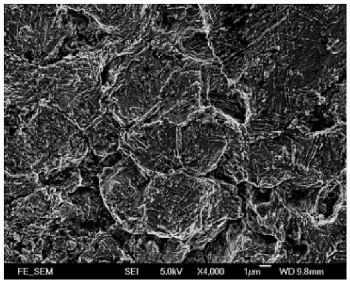

SEM micrograph showing damaged surface of MAB-Al-8 after 12 h of erosion test in 3.5% NaCl solution.

(*continued on next page*)

Table 7 (*continued*)

[33] DN18. Cast NAB	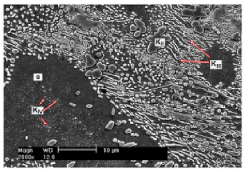	Microstructure of Ni-Al bronze
	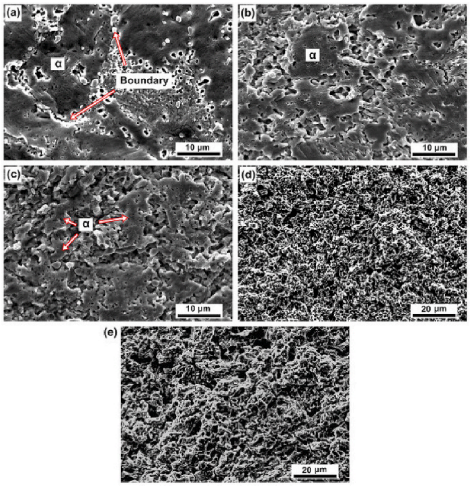	Surface morphologies of Ni-Al bronze with different CE time in 2.4 wt% NaCl solution **(a)** 10 min, **(b)** 30 min, **(c)** 1 h, **(d)** 3 h and **(e)** 6 h.
[34], DN19&20 Forged and cast NAB	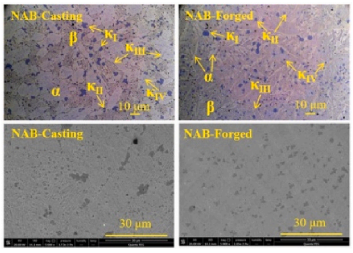	OM and SEM images of polished NABs.
	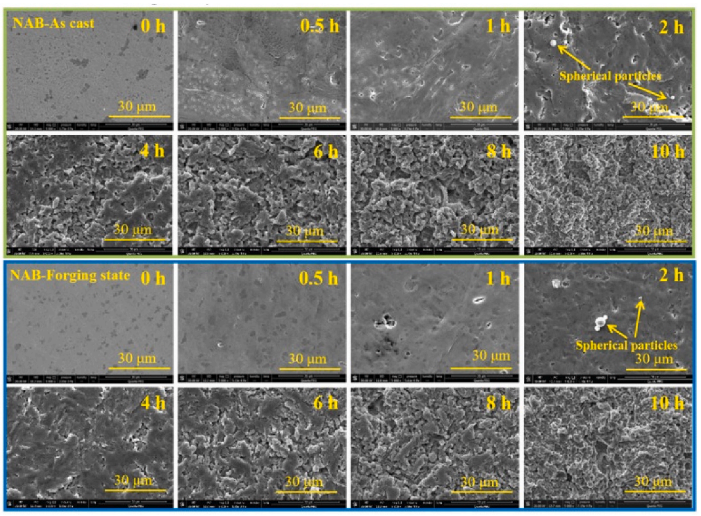	SEM images of the surfaces of NAB-Casting and NAB-Forged after different CE time in artificial seawater.

(*continued on next page*)

Table 7 (*continued*)

[35] DN21 Cast NAB	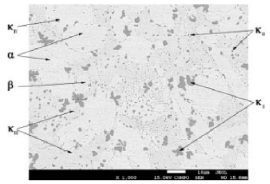 SEM image of the microstructure of as-cast NAB alloy.

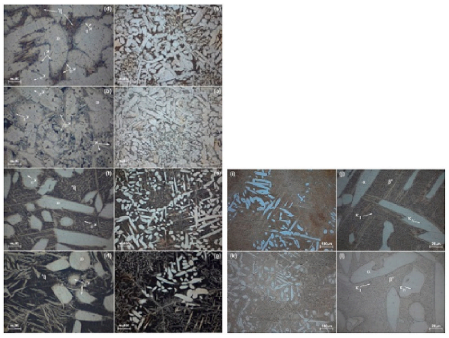

Microstructure of NAB alloys under different heat treatments. **(a)** and **(b)**: as-cast NAB; **(c)** and **(d)**: annealing at 675 °C; (e) and (f): normalizing at 900 °C; **(g)** and **(h)**: quenching and aging at 450 °C; **(i)** and **(j)**: quenching and aging at 550 °C; **(k)** and **(l)**: quenching and aging at 650 °C.

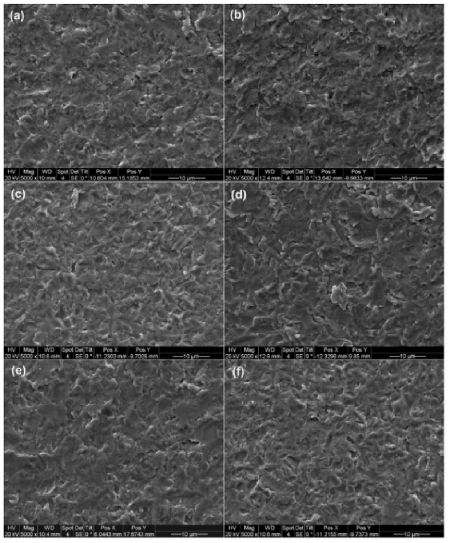

Worn surfaces of NAB alloys under different heat treatments upon erosion–corrosion testing. **(a)** As-cast alloy; (b) annealing at 675 °C; (c) normalizing at 900 °C; (d) quenching and aging at 450 °C; (e) quenching and aging at 550 °C; (f) quenching and aging at 650 °C (conditions: 3.5 wt% NaCl, 3 wt% sand, 5.0 m s^{-1}, and 5 h).

(*continued on next page*)

Table 7 (*continued*)

[36], DN22 Cast NAB and hot extruded NAB	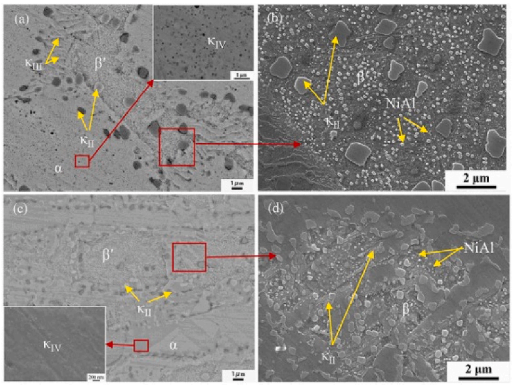 SEM microstructures of **(a, b)** AC-NAB and **(c, d)** Hot Extruded-NAB alloys No images of eroded surfaces available	
[37], DN23 Cast NAB and Friction Stir Processed (FSP) NAB	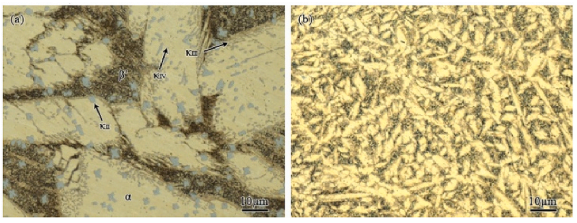 OM showing the microstructures of **(a)** as-cast NAB, **(b)** FSP NAB.	
	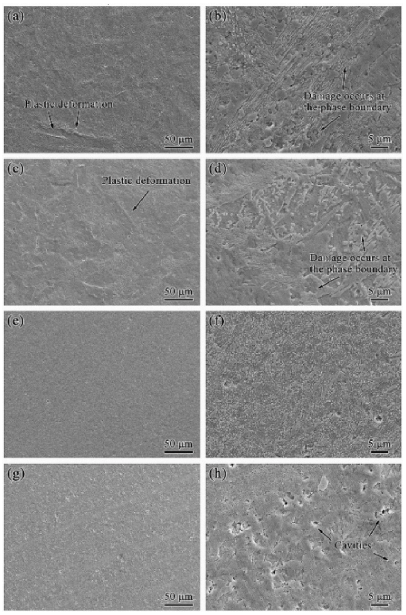 SEM images showing the morphological damage after cavitation erosion in **a**, **b**, **e**, **f** distilled water and **c**, **d**, **g**, **h** artificial seawater for 2 h: (**a**–**d**) as-cast NAB, (**e**–**h**) FSP NAB	

(*continued on next page*)

Table 7 (*continued*)

[38] DN24&25
Cast NAB and powder Metallurgy (PM) NAB and Heat treated (HT) NAB and HT-PM NAB

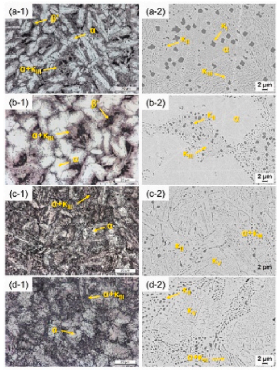

Microstructures of the studied NABs observed by OM (i-1) and SEM **(a)** cast; **(b)** PM; **(c)** HT-cast, **(d)** HT-PM.

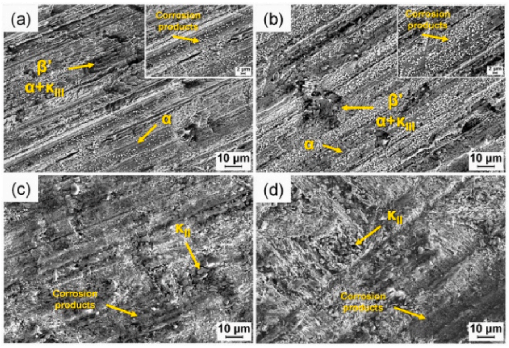

Surface morphology evolution of the as-cast NAB alloy after different immersion times in a slurry pot in 3.5 wt% NaCl solution. (a) 48 h; (b) 120 h; (c) 240 h; (d) 480 h

[22], DN27
Inconel 625
Hastelloy C-276

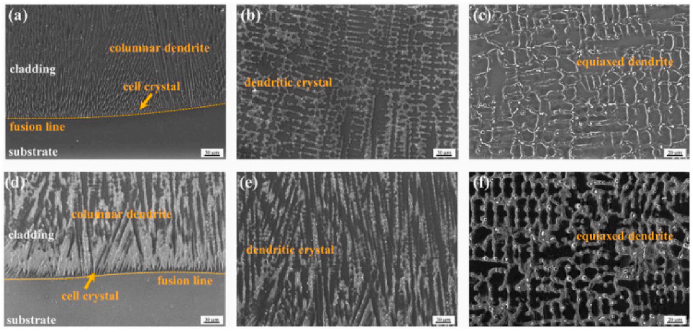

Inconel 625 coating: **(a)** at the coating/substrate interface **(b)** at the middle of the coating **(c)** near the surface; Hastelloy C-276 coating: **(d)** at the coating/substrate interface **(e)** at the middle of the coating **(f)** near the surface.

(*continued on next page*)

Table 7 (*continued*)

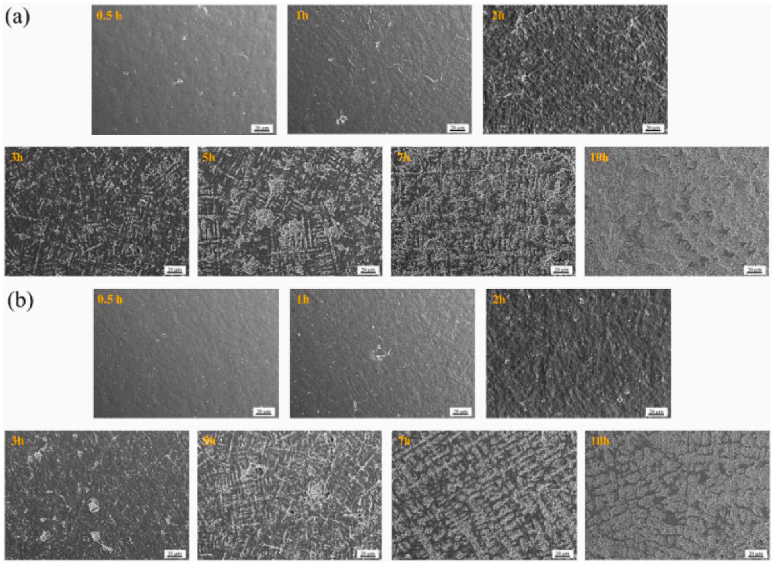

Morphology of the damaged surfaces after cavitation erosion as a function of time in 3.5 wt% NaCl solution of (a) Inconel 625 coating and (b) Hastelloy C-276 coating

Data availability

Data will be made available on request.

References

[1] J.A. Wharton, R.C. Barik, G. Kear, R.J.K. Wood, K.R. Stokes, F.C. Walsh, The corrosion of nickel–aluminium bronze in seawater, Corros. Sci. 47 (12) (2005/12/01) 3336–3367, https://doi.org/10.1016/j.corsci.2005.05.053, 2005.

[2] N.X. Qi-Ning Song, Yao Tong, Chen-Ming Huang, Shou-Yu Sun, Chen-Bo Xu, Ye-Feng Bao, Yong-Feng Jiang, Yan-Xin Qiao, Zhi-Yuan Zhu, Zheng-Bin Wang, Corrosion and cavitation erosion behaviours of cast nickel aluminium bronze in 3.5% NaCl solution with different sulphide concentrations, Acta Metall. Sin. 32 (12) (2019–12–10) 1470–1482, https://doi.org/10.1007/s40195-019-00963-7, 2019.

[3] H. Meigh, Cast and Wrought Aluminium Bronzes: Properties, Processes and Structure, first ed., CRC Press, 2000.

[4] Z. Qin, L. Cao, Y. Deng, Z. Cheng, W. Hu, Z. Wu, Effect of oxide film on the cavitation erosion-corrosion behavior of nickel-aluminum bronze alloy (in English), Corrosion 76 (12) (Dec 2020) 1136–1146, https://doi.org/10.5006/3348, 2020.

[5] Z. Qin, et al., Effect of compressive stress on cavitation erosion-corrosion behavior of nickel-aluminum bronze alloy (in eng), Ultrason. Sonochem. 89 (Sep 2022) 106143, https://doi.org/10.1016/j.ultsonch.2022.106143.

[6] T. Dobson, A. Yunnie, D. Kaloudis, N. Larrosa, H. Coules, Biofouling and corrosion rate of welded nickel aluminium bronze in natural and simulated seawater, Biofouling 40 (2) (2024/02/07) 193–208, https://doi.org/10.1080/08927014.2024.2326067, 2024.

[7] D.G. Li, S.L. Song, D.R. Chen, P. Liang, Effects of Ce, Sm and Yb on cavitation erosion of NAB alloy in 3.5% NaCl solution (in eng), Ultrason. Sonochem. 88 (Aug 2022) 106093, https://doi.org/10.1016/j.ultsonch.2022.106093.

[8] DEF STAN 02-747 Part 02 Issue 4, *Defence Standard 02-747 Part 02*, Defence Equipment and Support, UK Defence Standardization, Glasgow, 2024 [Online]. Available: https://www.dstan.mod.uk/[Online]. Available, https://www.dstan.mod.uk/.

[9] B.G. Ateya, E.A. Ashour, S.M. Sayed, Stress corrosion behavior of α-Aluminum bronze in saline water, Corrosion 50 (1) (1994) 20–25, https://doi.org/10.5006/1.3293490.

[10] A. Schüssler, H.E. Exner, The corrosion of nickel-aluminium bronzes in seawater—I. Protective layer formation and the passivation mechanism, Corros. Sci. 34 (11) (1993/11/01) 1793–1802, https://doi.org/10.1016/0010-938X(93)90017-B, 1993.

[11] P.R. Roberge, *Erosion-Corrosion Testing* (Corrosion Tesrting Made Easy), NACE International, 2004.

[12] A.H. Tuthill, Guidelines for the use of copper alloys ·in seawater, Mater. Perform. 26 (1987) 12–22.

[13] J.P. Ault, Erosion corrosion of nickel aluminum bronze in flowing seawater, in: CORROSION 1995, 1995, pp. 1–9, https://doi.org/10.5006/C1995-95281, vol. CORROSION 1995, doi: 10.5006/c1995-95281. [Online].

[14] N.K. Awad, E.A. Ashour, N.K. Allam, Unravelling the composition of the surface layers formed on Cu, Cu-Ni, Cu-Zn and Cu-Ni-Zn in clean and polluted environments, Appl. Surf. Sci. 346 (2015/08/15) 158–164, https://doi.org/10.1016/j.apsusc.2015.03.200, 2015.

[15] K. Rahmouni, M. Keddam, A. Srhiri, H. Takenouti, Corrosion of copper in 3% NaCl solution polluted by sulphide ions, Corros. Sci. 47 (12) (2005/12/01) 3249–3266, https://doi.org/10.1016/j.corsci.2005.06.017, 2005.

[16] L.E. Eiselstein, B.C. Syrett, S.S. Wing, R.D. Caligiuri, The accelerated corrosion of Cu Ni alloys in sulphide-polluted seawater: mechanism no. 2, Corros. Sci. 23 (3) (1983/01/01) 223–239, https://doi.org/10.1016/0010-938X(83)90104-X, 1983.

[17] S.M. Sayed, E.A. Ashour, G.I. Youssef, Effect of sulfide ions on the corrosion behaviour of Al–brass and Cu10Ni alloys in salt water, Mater. Chem. Phys. 78 (3) (2003/02/28) 825–834, https://doi.org/10.1016/S0254-0584(02)00411-X, 2003.

[18] S.J. Yuan, S.O. Pehkonen, Surface characterization and corrosion behavior of 70/30 Cu–Ni alloy in pristine and sulfide-containing simulated seawater, Corros. Sci. 49 (3) (2007/03/01) 1276–1304, https://doi.org/10.1016/j.corsci.2006.07.003, 2007.

[19] Q.-N. Song, et al., Corrosion and cavitation erosion behaviors of two marine propeller materials in clean and sulfide-polluted 3.5% NaCl solutions, Acta Metall. Sin. 30 (8) (2017/08/01) 712–720, https://doi.org/10.1007/s40195-017-0602-7, 2017.

[20] R.J.K. Wood, Erosion–corrosion interactions and their effect on marine and offshore materials, Wear 261 (9) (2006/11/20/2006) 1012–1023, https://doi.org/10.1016/j.wear.2006.03.033.

[21] J. Basumatary, R.J.K. Wood, Different methods of measuring synergy between cavitation erosion and corrosion for nickel aluminium bronze in 3.5% NaCl solution, Tribol. Int. 147 (2020/07/01) 104843, https://doi.org/10.1016/j.triboint.2017.08.006, 2020.

[22] T. Zhao, et al., Cavitation erosion/corrosion synergy and wear behaviors of nickel-based alloy coatings on 304 stainless steel prepared by cold metal transfer, Wear 510–511 (2022/12/15) 204510, https://doi.org/10.1016/j.wear.2022.204510, 2022.

[23] V. Dutta, L. Thakur, B. Singh, H. Vasudev, A study of erosion-corrosion behaviour of friction stir-processed chromium-reinforced NiAl bronze composite (in eng), Materials (Basel) 15 (15) (Aug 5 2022), https://doi.org/10.3390/ma15155401.

[24] W.-Y. Wang, W.-J. Zhang, G.-J. Huang, X.-J. Mi, Synergistic improvement of erosion-corrosion resistance and mechanical properties of nickel aluminium bronze alloy by the addition of Cr, Rare Met. 44 (1) (2025/01/01) 623–638, https://doi.org/10.1007/s12598-024-02835-1, 2025.

[25] L. Li, Y. Qiao, L. Zhang, A. Ma, R. Ma, Y. Zheng, Understanding the corrosion behavior of nickel-aluminum bronze induced by cavitation corrosion using electrochemical noise: selective phase corrosion and uniform corrosion (in eng), Materials (Basel) 16 (2) (Jan 10 2023), https://doi.org/10.3390/ma16020669.

[26] Z. He, et al., Erosion-corrosion behavior of Ni-Al-Cu coating on nickel-aluminium bronze alloy in 3.5 wt% NaCl solution, Corros. Sci. 238 (2024/09/01) 112380, https://doi.org/10.1016/j.corsci.2024.112380, 2024.

[27] W. Wang, W. Zhang, G. Huang, X. Mi, L. Huang, Effect of in-situ pre-soaking in seawater on the erosion-corrosion properties and micro-mechanism of nickel aluminium bronze alloy, Corros. Sci. 228 (2024/03/01) 111841, https://doi.org/10.1016/j.corsci.2024.111841, 2024.
[28] J. Basumatary, R.J.K. Wood, Synergistic effects of cavitation erosion and corrosion for nickel aluminium bronze with oxide film in 3.5% NaCl solution, Wear 376–377 (2017/04/15) 1286–1297, https://doi.org/10.1016/j.wear.2017.01.047, 2017.
[29] R. Keshavamurthy, P. Kuppahalli, P. Sriram, K. Sridhar, Effect of silicon addition on erosion-corrosion characteristics of high-tensile brasses, J. Inst. Eng.(India): Series D 104 (1) (2023/06/01) 155–169, https://doi.org/10.1007/s40033-022-00405-2, 2023.
[30] C. Xu, Y. Peng, L.-Y. Chen, T.-Y. Zhang, J.-J. Cheng, K.-H. Wang, Advanced cavitation erosion-corrosion resistance of nickel-aluminum bronze prepared by directed energy deposition, Corros. Sci. 231 (2024/05/01) 111982, https://doi.org/10.1016/j.corsci.2024.111982, 2024.
[31] C. Wang, et al., Erosion-corrosion behaviour of shot peening treated nickel-aluminium bronze in simulated sand-containing seawater, Corros. Sci. 211 (2023/02/01) 110908, https://doi.org/10.1016/j.corsci.2022.110908, 2023.
[32] C.H. Tang, F.T. Cheng, H.C. Man, Laser surface alloying of a marine propeller bronze using aluminium powder: part II: corrosion and erosion–corrosion synergism, Surf. Coating. Technol. 200 (8) (2006/01/24) 2594–2601, https://doi.org/10.1016/j.surfcoat.2004.12.022, 2006.
[33] L.M. Zhang, A.L. Ma, H. Yu, A.J. Umoh, Y.G. Zheng, Correlation of microstructure with cavitation erosion behaviour of a nickel-aluminum bronze in simulated seawater, Tribol. Int. 136 (2019/08/01) 250–258, https://doi.org/10.1016/j.triboint.2019.03.071, 2019.
[34] J. Ma, et al., Why does seawater corrosion significantly inhibit the cavitation erosion damage of nickel-aluminum bronze? Corros. Sci. 209 (2022/12/01/2022) 110700, https://doi.org/10.1016/j.corsci.2022.110700.
[35] Z. Wu, Y.F. Cheng, L. Liu, W. Lv, W. Hu, Effect of heat treatment on microstructure evolution and erosion–corrosion behavior of a nickel–aluminum bronze alloy in chloride solution, Corros. Sci. 98 (2015/09/01) 260–270, https://doi.org/10.1016/j.corsci.2015.05.037, 2015.
[36] W. Wang, et al., Tailoring microstructure of a nickel aluminium bronze by hot extrusion and its impact on mechanical and corrosion behaviour, Corros. Sci. 215 (2023/05/01) 111049, https://doi.org/10.1016/j.corsci.2023.111049, 2023.
[37] Y. Li, Y. Lian, Y. Sun, Synergistic effect between cavitation erosion and corrosion for friction stir processed NiAl bronze in artificial seawater, Met. Mater. Int. 27 (12) (2021/12/01) 5082–5094, https://doi.org/10.1007/s12540-020-00916-1, 2021.
[38] A. Fayanás, et al., Correlation between microstructure and erosion-corrosion behavior of a nickel-aluminum bronze produced by continuous casting and powder metallurgy, J. Mater. Res. Technol. 36 (2025/05/01) 3818–3830, https://doi.org/10.1016/j.jmrt.2025.04.009, 2025.
[39] T. Hodgkiess, G. Vassiliou, Complexities in the erosion corrosion of copper-nickel alloys in saline water, Desalination 183 (1) (2005/11/01) 235–247, https://doi.org/10.1016/j.desal.2005.03.037, 2005.
[40] ASTM G32-16(2021)e1, Standard Test Method for Cavitation Erosion Using Vibratory Apparatus, ASTM, West Conshohocken, PA, USA, 2016, https://doi.org/10.1520/G0032-16R21E01.
[41] A.K. Lakshminarayanan, S.R.K. Rao, K. Sridhar, A. Vignesh, On the microstructure and erosion corrosion behavior of laser processed nickel aluminium bronze, Mater. Sci. Forum 979 (2020) 157–161. https://doi.org/10.4028/www.scientific.net/MSF.979.157.
[42] R.C. Barik, J.A. Wharton, R.J.K. Wood, K.S. Tan, K.R. Stokes, Erosion and erosion–corrosion performance of cast and thermally sprayed nickel–aluminium bronze, Wear 259 (1) (2005/07/01) 230–242, https://doi.org/10.1016/j.wear.2005.02.033, 2005.
[43] M. Lotfollahi, M. Shamanian, A. Saatchi, Effect of friction stir processing on erosion–corrosion behavior of nickel–aluminum bronze, Mater. Des. (1980-2015) 62 (2014/10/01) 282–287, https://doi.org/10.1016/j.matdes.2014.05.037, 2014.
[44] D.M. Kumar, Investigating the Synergistic Effects of Cavitation Erosion-Corrosion for Nickel Aluminium Bronze with Air-Oxide Film and Anodic Oxide Film in 3.5% NaCl, University of Southampton, 2024. Third year project report May 2024.
[45] M. Hazra, K.P. Balan, Failure of a nickel aluminium bronze (NAB) canned motor pump impeller working under polluted sea water – influence of material selection, section thickness dependent microstructure and temper annealing heat treatment, Eng. Fail. Anal. 70 (2016/12/01) 141–156, https://doi.org/10.1016/j.engfailanal.2016.07.010, 2016.
[46] L. Shizhuo, J. Xiaoxia, B. Hongyun, L. Shu, Effect of environmental embrittlement on wear resistance of alloys in corrosive wear, Wear 225–229 (1999/04/01) 1025–1030, https://doi.org/10.1016/S0043-1648(99)00079-4, 1999.
[47] H.Y. Al-Fadhli, J. Stokes, M.S.J. Hashmi, B.S. Yilbas, The erosion–corrosion behaviour of high velocity oxy-fuel (HVOF) thermally sprayed inconel-625 coatings on different metallic surfaces, Surf. Coating. Technol. 200 (20) (2006/05/22) 5782–5788, https://doi.org/10.1016/j.surfcoat.2005.08.143, 2006.
[48] F. Brownlie, T. Hodgkiess, A. Pearson, A.M. Galloway, A study on the erosion-corrosion behaviour of engineering materials used in the geothermal industry, Wear 477 (2021/07/18) 203821, https://doi.org/10.1016/j.wear.2021.203821, 2021.
[49] R.J.K. Wood, S.P. Hutton, The synergistic effect of erosion and corrosion: trends in published results, Wear 140 (2) (1990/11/01) 387–394, https://doi.org/10.1016/0043-1648(90)90098-U, 1990.
[50] W.J. Tomlinson, M.G. Talks, Cavitation erosion of grey cast irons containing 0.2 and 1.0% phosphorous in corrosive waters, Tribol. Int. 22 (3) (1989/06/01) 195–204, https://doi.org/10.1016/0301-679X(89)90157-6, 1989.
[51] D.M. Kumar, Investigating the Synergistic Effects of Cavitation Erosion-Corrosion for Nickel Aluminium Bronze with Air-Oxide Film and Anodic Oxide Film in 3.5% NaCl, University of Southampton, 2024 in "Third year report," Univerity of Southampton.